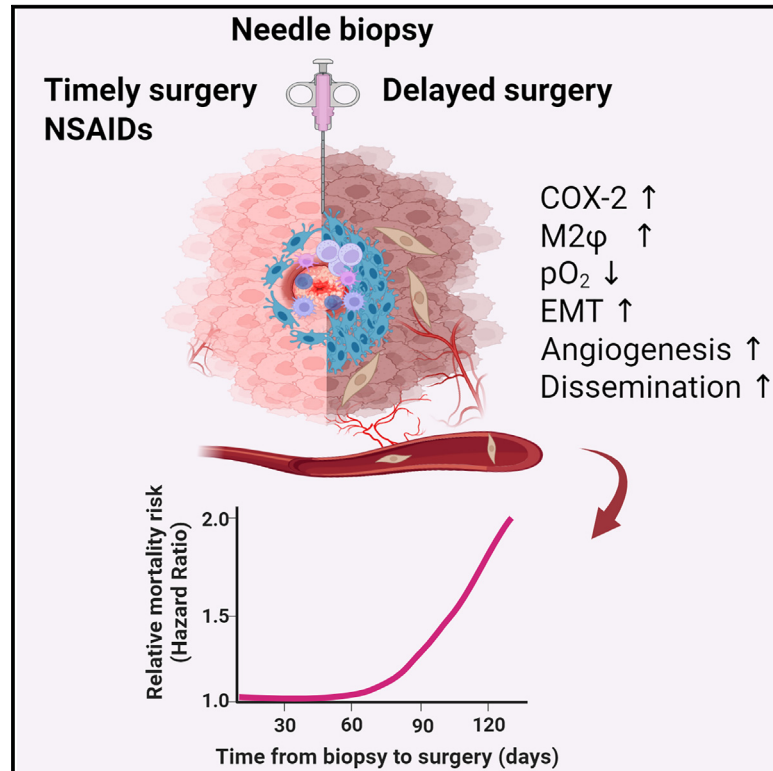**Article**

Needle biopsy accelerates pro-metastatic changes and systemic dissemination in breast cancer: Implications for mortality by surgery delay

Graphical abstract

Authors

Hiroyasu Kameyama, Priya Dondapati, Reese Simmons, ..., Inna Chervoneva, Hallgeir Rui, Takemi Tanaka

Correspondence

takemi-tanaka@ouhsc.edu

In brief

Kameyama and colleagues reveal that needle biopsy of breast tumors instigates pro-metastatic progression and systemic dissemination through protracted activation of COX-2 and M2φ paracrine factors, while oral NSAIDs mitigate these effects. These data may explain the increased mortality risk posed by surgery delay after diagnostic biopsy in early-stage breast cancer.

Highlights

- Delay of surgery after a diagnostic biopsy is associated with increased mortality

- Biopsied tumors retain a M2φ-dominant wound capable of pro-metastatic progression

- Core needle biopsy of breast tumors enhances cancer cell dissemination

- Oral NSAIDs mitigate biopsy-associated pro-metastatic progression and dissemination

CellPress

Article

Needle biopsy accelerates pro-metastatic changes and systemic dissemination in breast cancer: Implications for mortality by surgery delay

Hiroyasu Kameyama,[1] Priya Dondapati,[1] Reese Simmons,[1] Macall Leslie,[1] John F. Langenheim,[2] Yunguang Sun,[3] Misung Yi,[4] Aubrey Rottschaefer,[1] Rashmi Pathak,[1] Shreya Nuguri,[1] Kar-Ming Fung,[5] Shirng-Wern Tsaih,[6] Inna Chervoneva,[4] Hallgeir Rui,[2] and Takemi Tanaka[1,5,7,*]

[1]Stephenson Cancer Center, University of Oklahoma Health Sciences Center, 975 NE 10th St., Oklahoma City, OK 73104, USA
[2]Department of Pharmacology, Physiology & Cancer Biology, Sidney Kimmel Cancer Center, Thomas Jefferson University, 233 S 10th St., BLSB 1008, Philadelphia, PA 19107, USA
[3]Department of Pathology, Medical College of Wisconsin, 8701 Watertown Plank Road, Milwaukee, WI 53226, USA
[4]Division of Biostatistics, Department of Pharmacology, Physiology & Cancer Biology, Sidney Kimmel Cancer Center, Thomas Jefferson University, 233 S 10th St., BLSB 1008, Philadelphia, PA 19107, USA
[5]Department of Pathology, School of Medicine, University of Oklahoma Health Sciences Center, 940 Stanton L Young Boulevard, Oklahoma City, OK 73104, USA
[6]Department of Obstetrics and Gynecology, Medical College of Wisconsin, 8701 Watertown Plank Road, Milwaukee, WI 53226, USA
[7]Lead contact
*Correspondence: takemi-tanaka@ouhsc.edu
https://doi.org/10.1016/j.xcrm.2023.101330

SUMMARY

Increased breast cancer (BC) mortality risk posed by delayed surgical resection of tumor after diagnosis is a growing concern, yet the underlying mechanisms remain unknown. Our cohort analyses of early-stage BC patients reveal the emergence of a significantly rising mortality risk when the biopsy-to-surgery interval was extended beyond 53 days. Additionally, histology of post-biopsy tumors shows prolonged retention of a metastasis-permissive wound stroma dominated by M2-like macrophages capable of promoting cancer cell epithelial-to-mesenchymal transition and angiogenesis. We show that needle biopsy promotes systemic dissemination of cancer cells through a mechanism of sustained activation of the COX-2/PGE$_2$/EP2 feedforward loop, which favors M2 polarization and its associated pro-metastatic changes but are abrogated by oral treatment with COX-2 or EP2 inhibitors in estrogen-receptor-positive (ER$^+$) syngeneic mouse tumor models. Therefore, we conclude that needle biopsy of ER$^+$ BC provokes progressive pro-metastatic changes, which may explain the mortality risk posed by surgery delay after diagnosis.

INTRODUCTION

Breast cancer (BC) is the most commonly diagnosed malignancy in the United States.[1] Over two-thirds of invasive BC cases are diagnosed early while the tumor is still relatively small and operable.[2] However, 15-year survival rates for early-stage BC remain in the range of 70%–77%.[3,4] A meta-analysis has documented that delay of surgery after diagnosis is associated with an increased risk of death in different cancer types.[5] In particular, studies showed an increased risk of disease progression[6] and mortality[7] among early-stage BC patients whose surgery was delayed over 60 days after the diagnostic biopsy. These and other observations[8–10] provided the rationale for the 2022 Commission on Cancer recommendation that patients with clinical stage I–III BC in the non-neoadjuvant setting should receive the first therapeutic surgery within 60 days of the diagnostic biopsy.[11] However, the mechanism(s) underlying the rapidly increased mortality due to delay of surgery after diagnosis remain unknown.

The biopsy-to-surgery interval was created incidentally as a consequence of needle biopsy gradually replacing open surgical excisional biopsies followed by same-day surgery as the preferred method of diagnosis.[12] Currently, core needle biopsy using 8- to 21-gauge needles with or without vacuum assistance is the mainstay for accurate clinical diagnoses in an era of high-volume referrals for mammography-detected suspicious lesions.[13,14] Safety studies conducted during the 1960s–1980s showed that needle biopsy of malignant breast tumors did not affect mortality when compared to excisional biopsies.[15,16] However, these studies were limited to short biopsy-to-surgery intervals (range of 7–30 days). Over the past decades, the biopsy-to-surgery interval for BC has grown substantially in the United States.[7,8,17,18] Such delay of first-line therapeutic surgery allows additional days of disease progression to occur. However, considering the established multi-year timescale of tumor development and slow progression of most invasive BC,[19,20] we explored alternative explanations that may underlie the conspicuous acceleration in disease progression and subsequent

increased mortality risk in a just over 60-day time window following diagnostic biopsy.

Needle biopsy injures tumor tissue, inducing wound-healing-related changes within the tumor.[21–24] We previously reported that more than 70% of stage I–II BC specimens display a disproportionate prevalence of macrophages (Mφ) adjacent to the biopsy needle tract compared to more distant tumor regions regardless of the biopsy-to-surgery interval.[24] Significant functional overlap has been described between anti-inflammatory Mφ involved in wound resolution (M2φ or so-called M2a) and tumor-associated macrophages with M2-like phenotype (M2-TAMs),[25,26] both of which produce potent soluble factors that induce angiogenesis, proliferation, epithelial-to-mesenchymal transition (EMT), and extracellular matrix remodeling.[27,28] We therefore hypothesized that needle biopsy introduces an M2φ-dominant wound stroma, rich in pro-metastatic paracrine factors, which stimulates pro-metastatic progression and systemic dissemination of cancer cells.

Here, we present several lines of evidence supporting biopsy-induced pro-metastatic effects as a biological mechanism underpinning the increased mortality risk associated with a prolonged biopsy-to-surgery interval in patients with early-stage BC. First, modeling propensity-score-adjusted mortality risk as a function of continuous biopsy-to-surgery interval in a large BC cohort revealed the delayed emergence of a significant increase in mortality risk when surgery was performed ≥53 days after biopsy. Second, histology of biopsied estrogen-receptor-positive (ER⁺) clinical and syngeneic mouse breast tumors, combined with experimental *in vitro* and *in vivo* approaches, supported the notion of sustained biopsy wound-induced expression of cyclooxygenase-2 (COX-2) and its enzymatic byproduct prostaglandin E_2 (PGE$_2$) in tumors which promote robust M2φ polarization via E-type prostanoid 2 (EP2) receptor, in turn promoting angiogenesis, cancer cell EMT, and systemic dissemination. Lastly, the administration of selective inhibitors for COX-2 or EP2 abrogated biopsy-induced metastasis in mice by disrupting the COX-2/PGE$_2$/EP2 feedforward loop.

RESULTS

Delayed emergence of rising mortality risk in early-stage breast cancer following diagnostic biopsy

Substantial evidence supports increased BC mortality risk with a prolonged biopsy-to-surgery interval.[5,8–10] However, the predominant approach using comparisons between sequential categories of biopsy-to-surgery interval (e.g., monthly or bimonthly) employed in previously published studies does not provide biological insight into how BC mortality risk increases rapidly after diagnosis. To investigate the hypothesis that diagnostic needle biopsy provokes pro-metastatic disease progression, which may underlie the increased mortality risk associated with prolonged biopsy-to-surgery intervals, we performed a cohort analysis by modeling mortality risk in relation to the biopsy-to-surgery interval as a continuous variable relative to a reference point (biopsy-to-surgery interval of 30 days) for stage I–II BC patients diagnosed by needle biopsy and who received surgery as their first treatment between 2007 and 2017 using the National Cancer Database (n = 176,481; Table S1). The flexible propensity

score-adjusted B-spline model delineated a biphasic trajectory of mortality risk. An initial lag-phase of 43 days without a detectable increase in mortality risk shifted to an increasing trend in risk thereafter, reaching significance at 53 days, and was followed by a second phase of exponential increase in mortality risk (Figure 1A), with 6%, 29%, 66%, and 117% higher mortality risk for patients who had a biopsy-to-surgery interval of 60, 90, 120, and 150 days, respectively, compared to the reference group who waited only 30 days for surgery (Figure 1B). The 14-year mortality was computed as 5%, 24%, and 54% higher for patients with biopsy-to-surgery intervals of 60, 90, and 120 days, respectively, compared to 16% for those with 30 days, indicating that delayed patients are at heightened risk throughout the follow-up period (Figure 1C). The observed biphasic trajectory with a delayed increase in mortality risk revealed that stage I–II BC undergoes accelerated disease progression after diagnosis rather than the constant rise in mortality risk from the time of diagnosis that would be expected simply from natural disease progression. Given the large volume of early-stage BC diagnoses each year and the steady rise in the median biopsy-to-surgery interval (Table S2),[7,8,17,18,29] mortality-risk increase associated with surgery delay is a substantial clinical problem.

Needle biopsy of breast tumors promotes systemic dissemination of BC cells in mouse models of ER⁺ BC

The cohort of patients with stage I–II BC examined from the National Cancer Database comprised over 87% ER⁺ diseases, among which 95% received adjuvant endocrine therapy (Table S2). The 15-year risk of ER⁺ BC mortality due to distant recurrence after completion of adjuvant endocrine therapy remains above 20%,[3,4] yet the mechanisms of distant recurrence of generally good prognostic indolent nature of ER⁺ BC remains unknown. Thus, we explored whether needle biopsy of tumors (a preoperative process essential for diagnosis of malignancy) may trigger disease progression conducive to systemic dissemination. To reflect the high frequency of recurrence in patients with early-stage ER⁺ BC, we enumerated disseminated cancer cells from whole lungs following tumor biopsy by employing two low-metastatic syngeneic mouse models of ER⁺ BC derived from epithelial-like Py230 and Py2T mouse mammary carcinoma cell lines with different strain backgrounds. Py230 or Py2T cells stably transduced with an mCherry reporter gene were orthotopically injected into the mammary glands of 6-week-old female B6 or FVB mice, respectively (Figure S1A). Size-matched mammary tumors of ~100 mm³ were biopsied once using a 22-gauge needle with vacuum assistance or left unbiopsied, and the lungs were isolated 15 days later (Figure 1D). Enumeration of mCherry⁺ cancer cells by flow cytometry of single-cell suspension from dissociated lungs showed a significantly higher number of disseminated cancer cells in biopsied mice than in unbiopsied controls, both in the Py230^mCherry (Figure 1E) and the Py2T^mCherry (Figure 1F) tumor models. Immunohistochemistry (IHC) staining for mCherry protein confirmed the presence of small metastatic foci and single cancer cells in the lung parenchyma of biopsied mice. Additional IHC staining of biopsied breast tumors showed spindle-shaped mCherry⁺ cancer cells
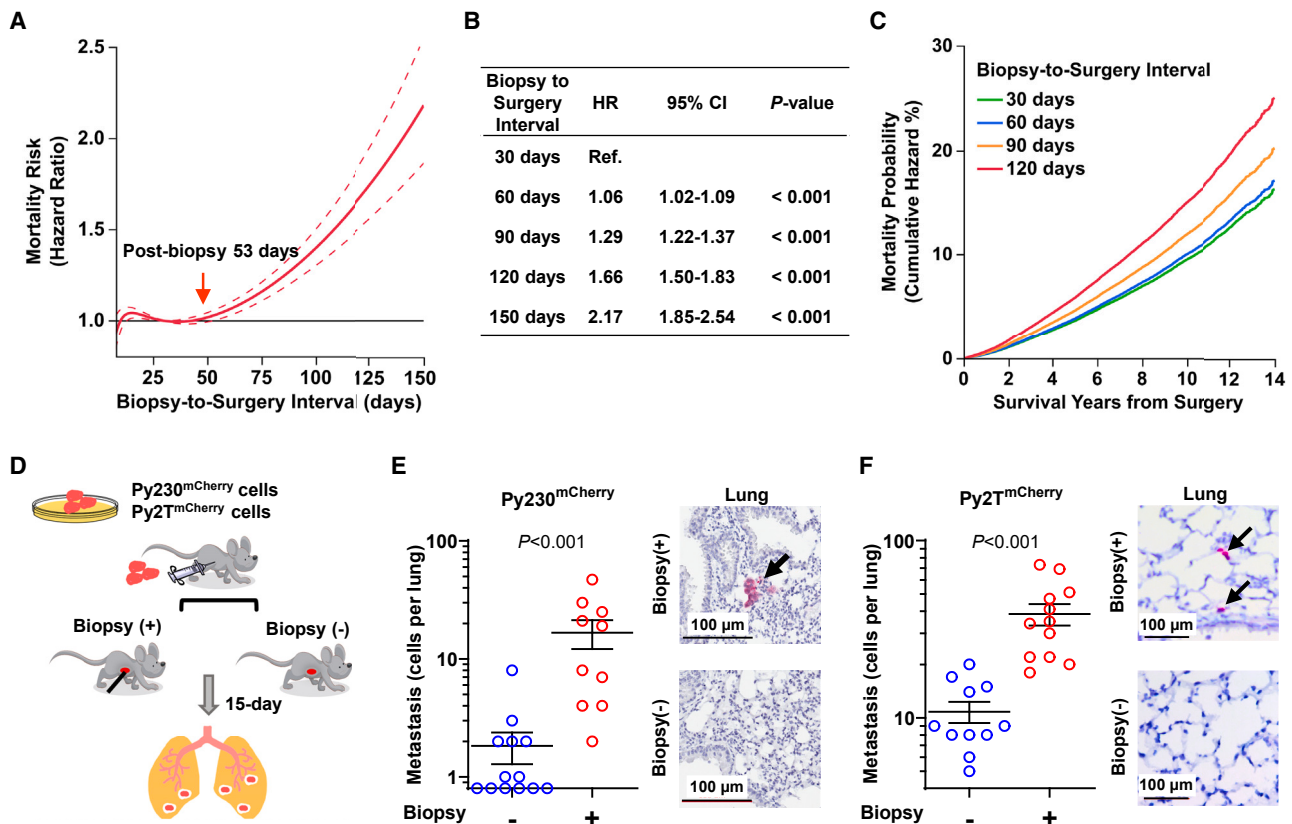
Figure 1. Needle biopsy of breast tumor promotes systemic dissemination

(A) Propensity-score-adjusted overall mortality risk with confidence interval (95% CI; dotted lines) plotted across the biopsy-to-surgery interval relative to the reference (30 days).

(B) Summary of hazard ratio (HR) at different biopsy-to-surgery intervals. Hazard ratios were computed with day 30 as the reference and simultaneous 95% CI; p values were adjusted for multiple comparisons using the Scheffe method.

(C) Overall mortality was plotted across the follow-up time (survival years) of patients with biopsy-to-surgery time intervals of 30, 60, 90, and 120 days.

(D) Schematic representation of biopsy-induced metastasis. Py230^{mCherry} or Py2T^{mCherry} mouse BC cells were injected into the abdominal mammary gland of B6 or FVB female mice, respectively. The tumors were biopsied once after reaching a size of 100 mm^3 or left unbiopsied, and the lungs were collected 15 days later.

(E and F) Detection of metastatic BC cells in the lungs of unbiopsied and biopsied mice using flow cytometry and immunohistochemistry. The number of Py230^{mCherry} (E) and Py2T^{mCherry} (F) metastatic cells in the lungs of unbiopsied (blue circles) and biopsied (red circles) mice after enzymatic dissociation and flow-cytometric analysis. Graphs represent mean ± SEM; p values were calculated using Wilcoxon test (n = 10–13 in Py230; n = 11–12 in Py2T). Representative images of lungs immunohistochemically stained for mCherry (red) showing metastatic BC cells (black arrow) in the lung parenchyma of mice with or without biopsy are shown.

around the biopsy wound in both Py230^{mCherry} and Py2T^{mCherry} tumors, suggesting the acquisition of mesenchymal-like phenotype (Figure S1B). Importantly, the tumor growth rate was unaffected by biopsy in both models (Figure S1C); Py230^{mCherry} cells were not detected in the circulation 6 h after the tumor biopsy (Figure S1D), indicating that aberrant tumor growth or forced dissemination of cancer cells due to needle insertion are unlikely causes of biopsy-induced systemic dissemination.

Needle biopsy promotes epithelial-to-mesenchymal transition of BC cells

Local invasion is a prerequisite for the systemic dissemination of cancer cells. In seeking possible mechanisms for biopsy-induced systemic dissemination, we postulated that needle biopsy of tumors promotes pro-metastatic phenotypic transition (i.e., EMT).[30–32] Twelve stage I–II, ER$^+$ clinical BC cases with a bi-

opsy-to-surgery interval ranging from 12 to 54 days (median 29.4 days) were histologically analyzed for the spatiotemporal prevalence of mesenchymal-like BC cells (Table S3A). A high-cellularity wound stroma was consistently present at the biopsy site of the surgically resected breast tumors that were examined, even after an extended time from biopsy (Figures 2A and S2A). Multiplex immunofluorescence revealed a significant loss of E-cadherin expression in singular or small clusters of pan-cyto-keratin-positive (CK$^+$) cancer cells adjacent to the biopsy wound, relative to CK$^+$ cancer cells distant from the biopsy wound (Figure 2A). The quantitative analysis documented that E-cadherin$^+$/CK$^+$ cells were disproportionately lower near the biopsy wound compared to distant areas (Figure 2B), and this reduced proportion with E-cadherin expression was consistently observed in all cases from as early as 12 days to as late as 54 days post biopsy (Figure 2C).
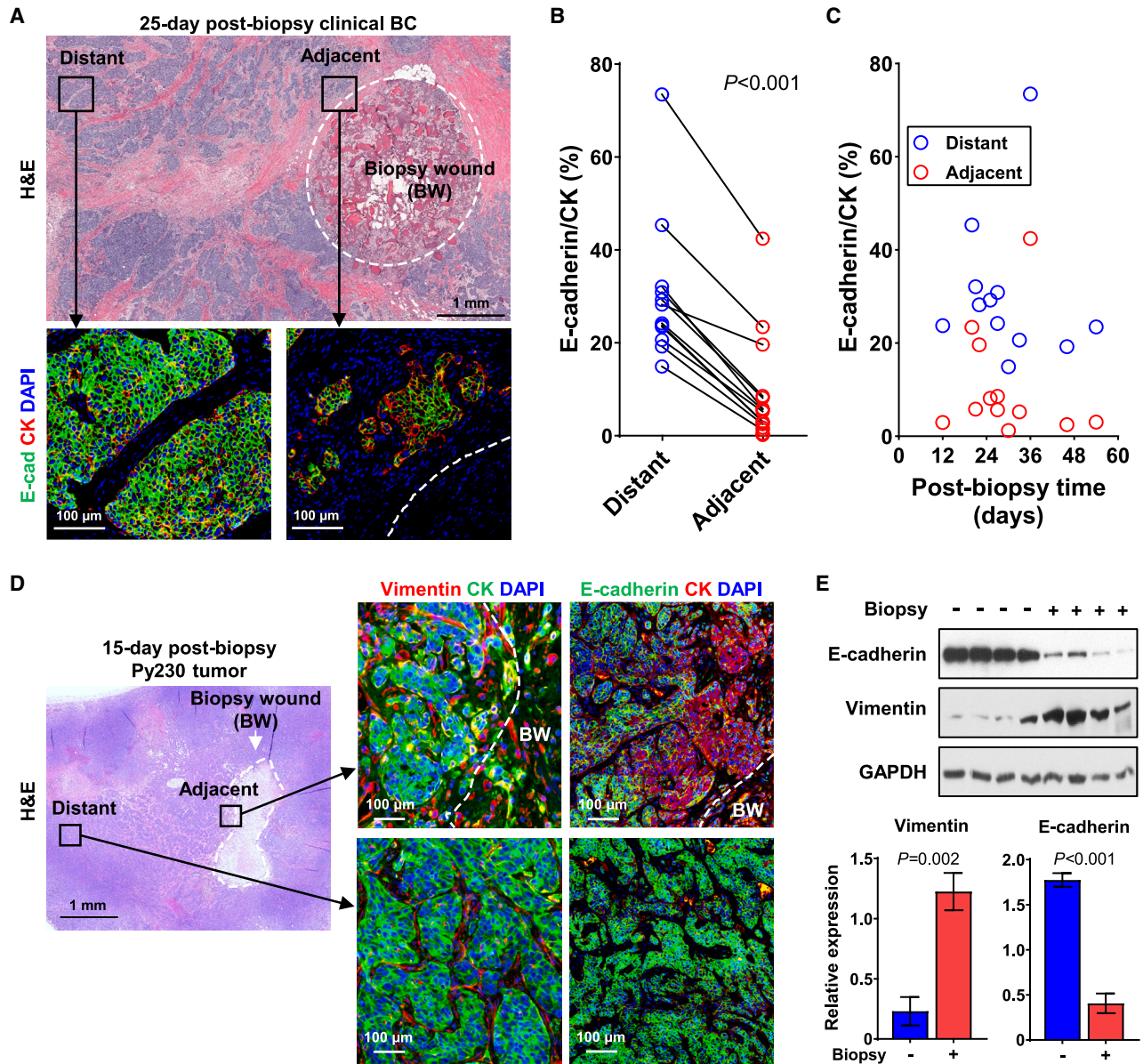
Figure 2. BC cells adjacent to the biopsy wound undergo epithelial-to-mesenchymal transition

(A) Representative images of surgically resected, 25-day post-biopsy ER$^+$, stage I clinical BC adjacent to and distant from the biopsy wound. Formalin-fixed paraffin-embedded sections were immunofluorescently stained for pan-CK (red) and E-cadherin (green) and counterstained with DAPI (blue). Black squares of biopsy-adjacent and -distant tumor regions in H&E image correspond to higher-power fluorescent images. The white dotted circle depicts the border of biopsy wound (BW).

(B) Paired line plot of the proportion of E-cadherin$^+$/CK$^+$ cells adjacent to (within 400 μm) and distant from (>3 mm away) the border of biopsy wound in 12 invasive ductal carcinomas. p values were calculated using the paired t test.

(C) Spatiotemporal mapping of E-cadherin$^+$/CK$^+$ cancer cells adjacent to and distant from the biopsy wound over various biopsy-to-surgery intervals.

(D) Representative images of Py230 tumors, adjacent to (<500 μm) or distant from (>2 mm away) the border of biopsy wound, are depicted by the white dotted line. 15-day post-biopsy tumors were immunofluorescently stained for pan-CK (green) and vimentin (red) in the left panel or pan-CK (red) and E-cadherin (green) in the right panel, counterstained with DAPI (blue).

(E) Western blot of E-cadherin and vimentin protein levels in whole tumor lysate of unbiopsied and 15-day post-biopsy Py230 tumors. The graph depicts the relative expression normalized by GAPDH (n = 4). The data are shown as mean ± SEM; p values were calculated using Student's t test.

Similar to the clinical BC, histology of 15-day post-biopsy Py230 mouse mammary tumors showed substantial accumulation of infiltrating stromal cells around the biopsy wound (Figures 2D and S2B). Vimentin expression was detected in CK$^+$ cancer cells adjacent to the biopsy wound in 15-day post-biopsy Py230 tumors but was rarely present in cancer cells

A 20-day post-biopsy clinical BC

B

C

D F4/80

CD206

E

F M1 M2 M2/M1

G

H
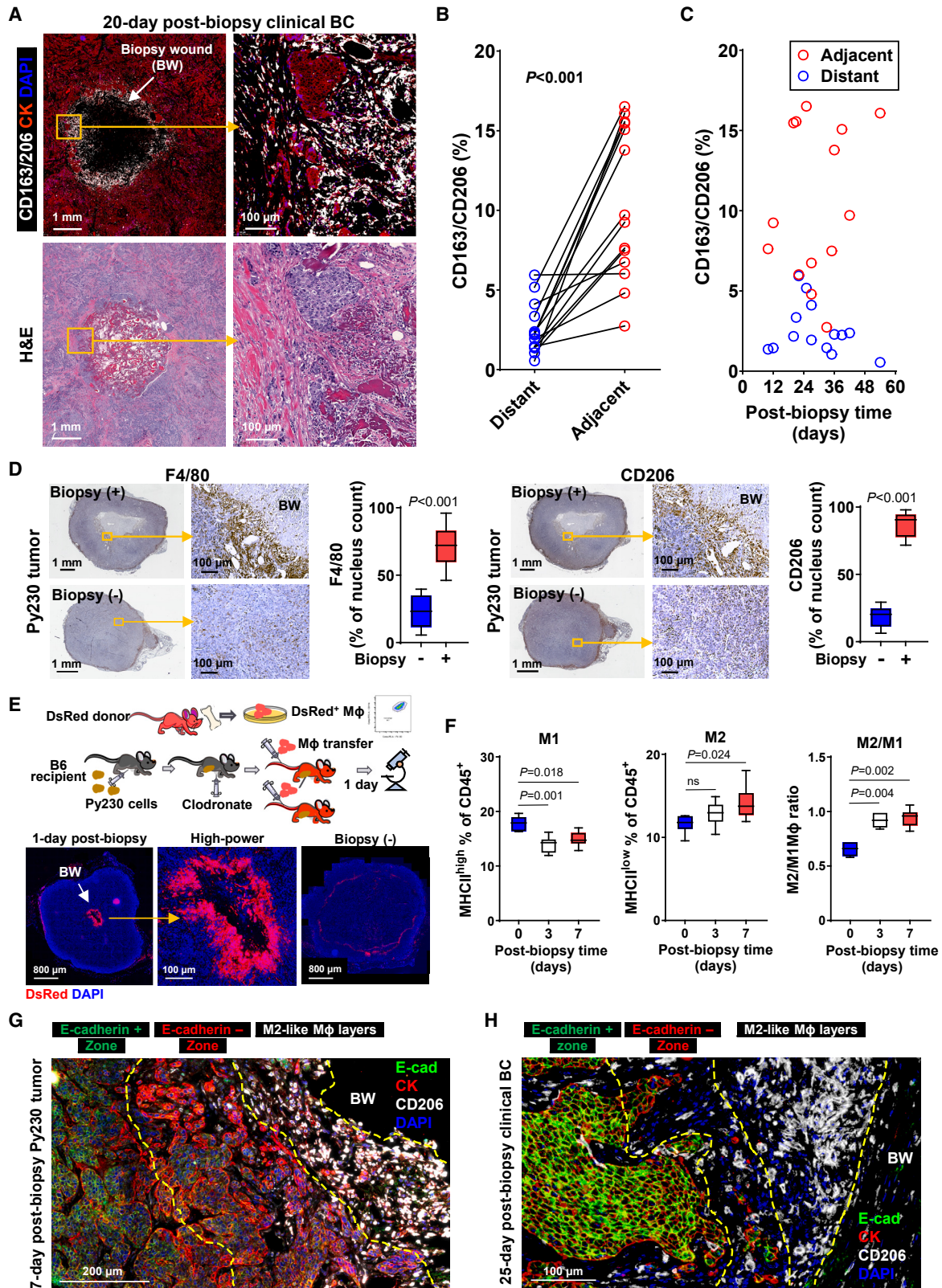
(legend on next page)

distant from it (Figure 2D). Vimentin[+]/CK^{+} cancer cells often displayed a spindle shape as either singular or small clusters. Consistent with clinical BC, substantial loss of E-cadherin expression was observed in CK^{+} cancer cells adjacent to the biopsy wound in Py230 tumors as early as 15 days post biopsy compared to CK^{+} cancer cells in distant areas (Figure 2D). Moreover, cancer cells adjacent to the biopsy wound expressed CK14 and CK17 (Figure S2C), basal cytokeratins that are often correlated with an aggressive phenotype and poor prognosis.[33,34] Furthermore, western blot analysis validated a significant reduction in E-cadherin and increased vimentin expression in the lysate of biopsied Py230 tumors compared to size-matched control tumors (Figure 2E). Collectively, the observed altered EMT marker expressions with concurrent spindle-shaped morphology suggested that cancer cells adjacent to the biopsy wound undergo EMT, indicative of the acquisition of invasive features.[35]

M2-like macrophages accumulate on the periphery of the biopsy wound

We have previously reported that macrophages (Mφ) are enriched adjacent to the biopsy wound compared to distant areas of surgically resected adjuvant-treated stage I–II breast tumors.[24] In wounds within healthy tissues, the Mφ phenotype readily changes based on spatiotemporal cues during healing, initially displaying a pro-inflammatory M1-like phenotype followed by a rapid transition into an anti-inflammatory M2-like phenotype. In seeking a mechanism for the observed cancer cell EMT near the biopsy wound, we performed multi-color immunofluorescence to determine whether infiltrating Mφ adjacent to the biopsy wound displayed an M2-like phenotype, known to promote cancer cell EMT.[32] In 14 stage I–II ER[+] clinical BC cases, with a median biopsy-to-surgery interval of 28.8 days (range 10–54 days; Table S3B), we consistently detected significant enrichment of M2-like Mφ positive for CD163 and/or CD206 markers around the biopsy wound, forming a ring-like structure on the interface between the biopsy wound and surrounding tumor parenchyma (Figure 3A). Intriguingly, M2-like Mφ were more abundant adjacent to the biopsy wound than in

distant areas (Figure 3B) and distributed across the entire range of biopsy-to-surgery interval lengths examined, as early as day 10 to as late as day 54 (Figure 3C). Generally, Mφ infiltration into a wound begins within a few hours of injury,[36] and baseline levels are restored within 10 days in mice.[37] Thus, the observed prolonged enrichment of M2-like Mφ in tumor biopsy wounds is deemed to reflect aberrant wound healing.[38]

Enrichment of M2φ around the biopsy wound was fully reproduced in biopsied Py230 tumors, with a 3- and 4.5-fold higher density of F4/80^{+} Mφ and CD206^{+} M2-like Mφ, respectively, compared to unbiopsied control tumors (Figure 3D) and randomly selected areas distant from the biopsy wound of matched tumors (Figure S3A). To validate spatiotemporal Mφ infiltration into the biopsy wound from the blood circulation, Mφ were isolated from femurs of female mice (Figure S3B). Freshly isolated Mφ from dsRed T3 mice[39] were adoptively transferred by intravenous injection into Mφ-depleted, Py230 tumor-bearing B6 recipient mice immediately prior to biopsy (Figure 3E). This adoptive transfer model revealed local enrichment of Mφ[DsRed] selectively around the biopsy wound within 24 h at levels far denser than in peripheral tumor stroma, based on direct imaging of unstained tumors (Figures 3E and S3C). We next confirmed that the infiltrating DsRed-labeled cells were M2 by documenting substantial overlap between direct immunofluorescent staining with fluorescein isothiocyanate-labeled CD206 antibody and DsRed fluorescence (Figure S3D), further supporting M2-like Mφ dominance within the biopsy wound. Fewer CD206^{+}/DsRed^{−} cells, presumably host M2φ, were scattered around the biopsy wound (Figure S3D). Furthermore, flow-cytometric analysis of the Mφ immunoprofile (Figure S3E) showed an inverse relationship with a reduction of CD45^{+}F4/80^{+}CD11b^{+}/CD11c^{−}MHC^{high} M1φ and an increase of CD45^{+}F4/80^{+}CD11b^{+}/CD11c^{−}MHCII^{low} M2φ from 3-day post-biopsy Py230 tumors and onward, leading to a significant elevation in the M2/M1 ratio (Figure 3F).

We have previously reported that close proximity of M2-like Mφ to cancer cells is an independent predictor of unfavorable prognosis in BC.[40] Thus, we investigated whether cancer cell EMT occurs adjacent to M2-like Mφ. Multi-color immunofluorescence of 7-day post-biopsy Py230 tumors showed a distinct

Figure 3. M2 macrophages accumulate adjacent to the biopsy wound and interface with nearby BC cells

(A) Representative images of 20-day post-biopsy, stage I, ER[+] breast tumor, immunofluorescently stained for CD163 and CD206 M2-like macrophages (white) and CK (red) and counterstained with DAPI (blue). The center hollow indicates the biopsy wound (BW). A high-power image corresponding to the yellow square displays the proximity of M2φ to cancer cells. H&E images show the corresponding areas.

(B) Paired line plot of the proportion of cells in tumor stroma adjacent to (<400 μm) and distant from (>3 mm away) the biopsy wound positive for CD163^{+}/CD206^{+} in 14 invasive ductal carcinomas. p values were calculated using the paired t test.
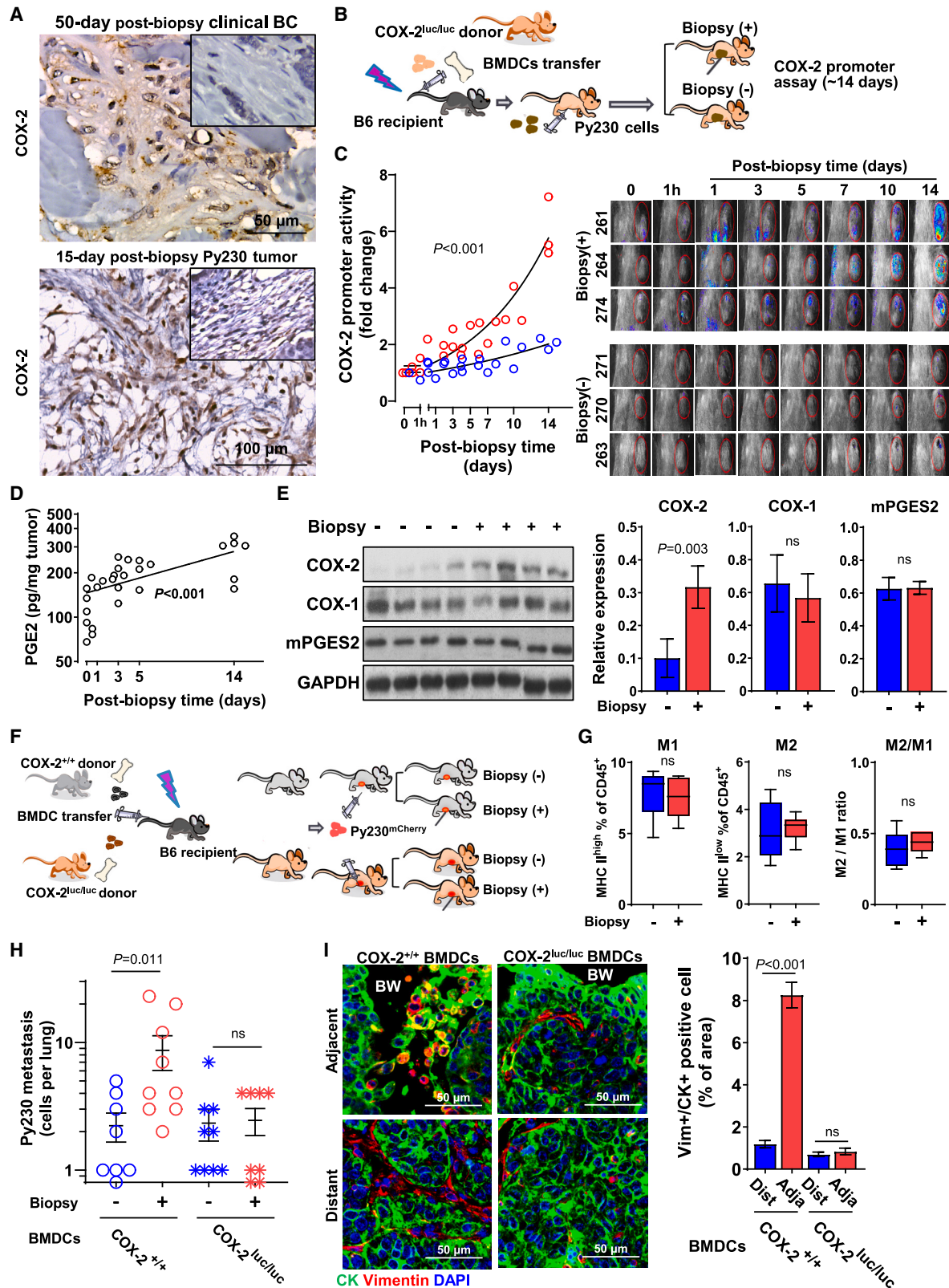
(C) Spatiotemporal mapping of CD163^{+}/CD206^{+} M2φ adjacent to and distant from the biopsy wound over various biopsy-to-surgery intervals.

(D) Representative images of 7-day post-biopsy or unbiopsied Py230 tumors, immunohistochemically stained for F4/80 and CD206 (brown) and counterstained with hematoxylin (blue). Yellow squares indicate the areas corresponding to the high-power images. The center oval of biopsied tumor images indicates the biopsy wound (BW). Graphs summarize the densities of F4/80^{+} or CD206^{+} normalized by nucleus count per field of view at 40× magnification. The data are shown as standard boxplots; p values were calculated using Wilcoxon test (n = 10).

(E) (Upper) Schematic illustration of experimental design for adoptive transfer of Mφ[DsRed]. (Lower) Fluorescent microscopic images of 1-day post-biopsy Py230 tumors in mice that received Mφ[DsRed] adoptive transfer at the time of biopsy (n = 6). The whole tumor and corresponding high-power images with the accumulation of Mφ[DsRed] (red) around the biopsy wound (center hollow circle) are shown. The slide was counterstained with DAPI (blue). BW, biopsy wound.

(F) Immunoprofile of Mφ isolated from Py230 tumors before or at various times after biopsy. Tumor biopsy reduces the proportion of M1φ (MHCII^{high}) and increases the proportion of M2φ (MHCII^{low}) and the ratio of M2φ to M1φ in CD45^{+} cells in the tumor. The data are shown as standard boxplots; p values were calculated using one-way ANOVA, relative to day 0 (n = 7–8).

(G and H) Representative images of 7-day post-biopsy Py230 tumors (G) and 25-day post-biopsy ER[+] clinical BC (H) adjacent to biopsy wound, immunofluorescently stained for CK (red), E-cadherin (green), and CD206 (white), and counterstained with DAPI (blue). The yellow dotted lines indicate the border of distinct zones outside the biopsy wound (BW).

A 50-day post-biopsy clinical BC

COX-2 — 50 μm

15-day post-biopsy Py230 tumor

COX-2 — 100 μm

B COX-2$^{luc/luc}$ donor
BMDCs transfer → Biopsy (+)
B6 recipient → Py230 cells → Biopsy (−)
COX-2 promoter assay (~14 days)

C COX-2 promoter activity (fold change) vs Post-biopsy time (days); $P<0.001$

Post-biopsy time (days): 0, 1h, 1, 3, 5, 7, 10, 14
Biopsy(+): 261, 264, 274
Biopsy(−): 271, 270, 263

D PGE2 (pg/mg tumor) vs Post-biopsy time (days); $P<0.001$

E Biopsy − − − − + + + +
COX-2, COX-1, mPGES2, GAPDH

COX-2 Relative expression; $P=0.003$; Biopsy − +
COX-1; ns; Biopsy − +
mPGES2; ns; Biopsy − +

F COX-2$^{+/+}$ donor
BMDC transfer
B6 recipient
COX-2$^{luc/luc}$ donor
→ Py230^{mCherry} → Biopsy (−), Biopsy (+)

G M1: MHC II^{high} % of CD45^{+}; ns; Biopsy − +
M2: MHC II^{low} % of CD45^{+}; ns; Biopsy − +
M2/M1: M2 / M1 ratio; ns; Biopsy − +

H Py230 metastasis (cells per lung); $P=0.011$; ns
Biopsy: − + − +
BMDCs: COX-2$^{+/+}$, COX-2$^{luc/luc}$

I COX-2$^{+/+}$ BMDCs | COX-2$^{luc/luc}$ BMDCs
Adjacent: BW | BW
Distant
CK Vimentin DAPI — 50 μm

Vim+/CK+ positive cell (% of area); $P<0.001$; ns
Dist, Adja | Dist, Adja
BMDCs: COX-2$^{+/+}$, COX-2$^{luc/luc}$

(legend on next page)

zonal distribution of mesenchymal phenotypes radiating outward from the biopsy wound with a multi-layer of CD206+ M2-like Mφ immediately outside the biopsy wound and a ~200- to 500-μm-deep layer of E-cadherin−/CK+ cancer cells with spindle-shaped single cells or small clusters outside the M2-like Mφ zone and encircled by E-cadherin+/CK+ cancer cells throughout the tumor distant from the biopsy wound (Figure 3G). Similarly, multiplex immunofluorescence of clinical BC showed juxtaposition of M2-like Mφ positive for CD163 and/or CD206 and small clusters of mesenchymal-like E-cadherin−/CK+ cancer cells within a 1-mm-deep zone surrounding the biopsy wound (Figure 3H). The emergence of a cancer cell EMT zone directly outside the M2φ layers in the biopsy wound milieu suggested EMT induction through local signaling from M2φ via TH2 paracrine factors.[41]

Tumor biopsy induces systemic cancer cell dissemination via cyclooxygenase-2

Because COX-2 is integral to the pro-inflammatory response in wound healing,[42] we investigated COX-2 expression in biopsied tumors. IHC staining showed substantially elevated COX-2 expression in infiltrating stromal cells of the biopsy cavity compared to peripheral stroma in both human and mouse tumors as late as 50 and 15 days post biopsy, respectively, suggesting protracted COX-2 activity within the biopsy wound stroma (Figures 4A and S4A). In contrast, the induction of COX-2 in cancer cells around the biopsy wound was absent (Figure S4B), while the baseline COX-2 expression level varied by case (Figure 4A). In wounds of healthy tissues, COX-2 expression rises transiently over the first few days after injury and rapidly subsides; thus, prolonged COX-2 expression implies a derailed wound-healing process. To temporally map COX-2 activation in the infiltrating stromal cells following biopsy, we performed adoptive transfer of bone marrow-derived cells (BMDCs) isolated from female *Cox-2* luciferase knockin/

knockout donor mice (*Cox-2[luc/luc]*)[43] to lethally irradiated recipient B6 mice. Following reconstitution, the recipient mice were orthotopically injected with Py230 cells, and the resulting tumors were biopsied when they reached ~100 mm³ in size or were left unbiopsied (Figure 4B). IVIS (*in vitro* information system) bioluminescent imaging detected an increase in *Cox-2* gene promoter activity in tumors as early as 1 h after biopsy (Figures 4C and S4C), which continued to rise exponentially throughout the study period of 14 days at a significantly higher rate than in unbiopsied tumors. The observed protracted and increasing *Cox-2* gene activity in infiltrating BMDCs in biopsied tumors was discordant with the transient nature of *Cox-2* gene activation. Tumor biopsy-induced prolonged activation of the *Cox-2* promoter was accompanied by continuous elevation of intratumoral PGE2 levels (Figure 4D). Western blot documented a 3-fold upregulation of COX-2 protein levels in biopsied Py230 tumors compared to unbiopsied controls (Figure 4E). In contrast, COX-1 and microsomal prostaglandin E synthase-2 (mPGES2; an enzyme responsible for the terminal synthesis of PGE2) protein levels remained unchanged (Figure 4E). These data provide evidence for aberrant activation of the COX-2/PGE2 axis in wound stroma in biopsied breast tumors. To examine the effect of COX-2 activation on biopsy-induced metastasis, following lethal irradiation, recipient mice received adoptive transfer of BMDCs from *Cox-2[luc/luc]* or wild-type (*Cox-2^{+/+}*) donor mice (Figure 4F). Py230 cells were orthotopically injected once reconstituted, after which tumors were either biopsied or left unbiopsied once they reached a size of ~100 mm³. Immunophenotypic profiling by flow-cytometric analysis of CD45+ cells dissociated from biopsied and unbiopsied Py230 tumors in mice adoptively transferred with BMDCs from *Cox-2[luc/luc]* showed no notable differences in the percentage of M1φ and M2φ and the M2φ/M1φ ratio (Figure 4G). Genetic deletion of *Cox-2* in the tumor-infiltrating BMDCs abrogated biopsy-induced Py230[mCherry] cancer cell dissemination to the lung (Figure 4H). Accordingly, EMT

Figure 4. Protracted activation of COX-2 in infiltrating BMDCs in biopsy wounds promotes EMT and systemic dissemination of BC

(A) Representative images of COX-2 staining of wound stroma cells in the biopsy cavity in 50-day post-biopsy stage I clinical BC and 15-day post-biopsy Py230 tumor. Insets indicate the distant stroma from the biopsy wound.

(B) Schematic diagram of experimental flow of *in vivo Cox-2* promoter assay. Six weeks following the adoptive transfer of BMDCs isolated from *Cox-2[luc/luc]* mice into lethally irradiated recipient mice, Py230 cells were orthotopically injected. Tumors were biopsied or left unbiopsied. Bioluminescence was detected immediately after intravenous injection of D-luciferin using an IVIS *in vivo* imaging system.

(C) *Cox-2* promoter activity at indicated times in individual mice that received biopsy (red) or left unbiopsied (blue). The graph depicts the fold change of total flux in the region of interest, relative to day 0 (before biopsy). Images depict bioluminescence on the tumor of individual mice over the experimental period. Data were analyzed in a linear mixed-effects model with random effects of mice and fixed effects of time after biopsy (n = 3).

(D) PGE2 quantification of Py230 tumors at the indicated times after biopsy using ELISA. Data were normalized by tumor weight and expressed as pg/mg tumor (n = 5). A simple linear regression was used to model the effect of time after biopsy on the levels of PGE2, relative to day 0. The curve was fitted using an exponential function.

(E) Western blot analysis of whole tumor lysate of Py230 tumors for COX-1, COX-2, and mPGES2 expression. The graph depicts the relative expression normalized by GAPDH (n = 4). The data are shown as mean ± SEM; p values were calculated using the Wilcoxon test, relative to the unbiopsied control.

(F) Schematic diagram of experimental flow of *Cox-2[luc/luc]* or *Cox-2^{+/+}* BMDC adoptive transfer. Six weeks following the adoptive transfer of BMDCs isolated from *Cox-2[luc/luc]* or *Cox-2^{+/+}* donor mice into lethally irradiated B6 recipient mice, Py230 cells were orthotopically injected. Tumors were biopsied or left unbiopsied and collected 15 days later.

(G) Immunoprofiling of Mφ phenotype of biopsied or unbiopsied Py230 tumors in *Cox-2[luc/luc]* recipients (n = 6). The data are shown as standard boxplots; p values were calculated using Wilcoxon test.

(H) Graph depicting the number of metastatic Py230[mCherry] cells in the lungs of *Cox-2[luc/luc]* and *Cox-2^{+/+}* recipients that were unbiopsied or biopsied (n = 8–9). Data were plotted as mean ± SEM and analyzed by two-way ANOVA, relative to unbiopsied control.

(I) Representative images of 15-day post-biopsy Py230 tumors adjacent to or distant from the biopsy wound, from *Cox-2[luc/luc]* and *Cox-2^{+/+}* recipients, immunofluorescently stained for CK (green) and vimentin (red) and counterstained with DAPI (blue). BW, biopsy wound. Graph on right summarizes the percentage of vimentin+/CK+ cells normalized by nucleus count per field of view at the final magnification of 40× (n = 5). The data are shown as mean ± SEM; p values were calculated using two-way ANOVA, relative to distant.
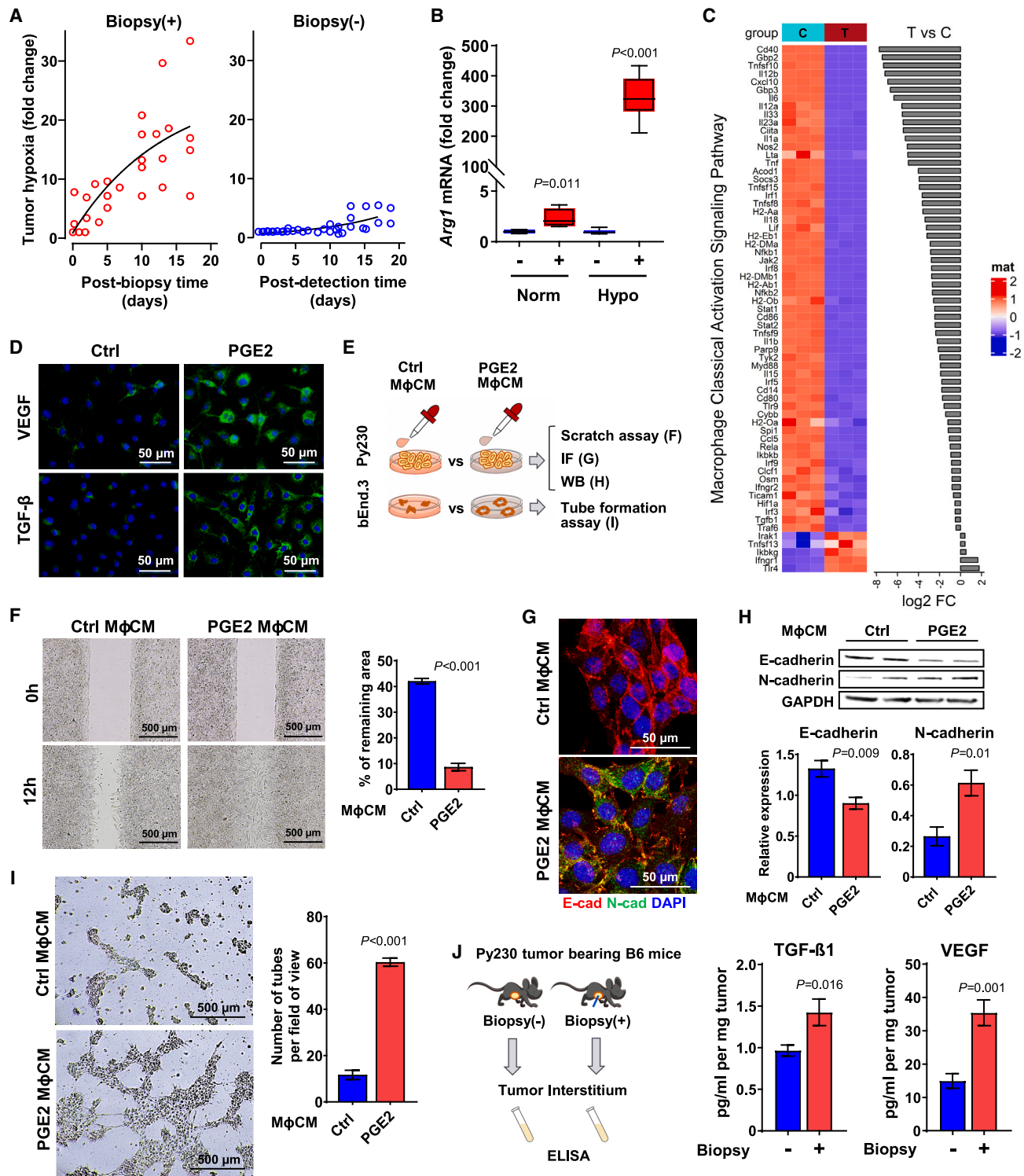
Figure 5. PGE₂ promotes M2 polarization under the hypoxic condition

(A) Tumor hypoxia was monitored longitudinally at indicated times from biopsied Py230 tumors (n = 5) or time-matched unbiopsied tumors (n = 6) using an IVIS *in vivo* imaging system and HypoxiSense 680 fluorescent probe. Time 0 indicates before biopsy. Regions of interest were quantified using Living Image software and are expressed in the graph as mean radiant efficiency over time. Data were analyzed in a linear mixed-effects model with random effects of mice and fixed effects of biopsy and time after biopsy.

adjacent to the biopsy wound retained a level similar to that distant from the wound in $Cox-2^{luc/luc}$ recipient mice (Figure 4I). Thus, these data suggest that continuous activation of COX-2/PGE$_2$ in the infiltrating stromal cells of the biopsy wound favors M2 shift, adjacent cancer cell EMT, and systemic dissemination of cancer cells.

PGE$_2$ promotes M2 polarization of Mφ under hypoxic conditions

We next explored whether PGE$_2$ contributes to M2 shift. To mimic the biopsy wound milieu *in vitro*, we first assessed the level of hypoxia of biopsied tumors, because wounds are typically oxygen deprived due to poor blood flow from disrupted vessels and high oxygen consumption of infiltrating cells.[44,45] *In vivo* monitoring of hypoxia in Py230 tumors using the HypoxySense 680 fluorescent probe by IVIS revealed a rapid and sustained biopsy-induced rise in carbonic anhydrase IX expression, with minimal increase over time in the unbiopsied control tumors (Figures 5A and S5A). Additional IHC staining with pimonidazole confirmed that biopsy-induced hypoxia was confined to the periphery of the biopsy wound, with a higher level in biopsied tumors compared to unbiopsied control tumors (Figure S5B). Exposure of bone marrow-derived primary Mφ to PGE$_2$ under hypoxia stimulated mRNA expression of the common M2 marker, arginase-1 (*Arg1*), more than 300-fold above levels observed under normoxic conditions (Figure 5B) as well as Arginase-1 protein (Figure S5C), suggesting a synergy between hypoxia and PGE$_2$ on M2 polarization. RNA-sequencing analysis for the polarization signatures of PGE$_2$-treated Mφ vs. control Mφ under hypoxia revealed 9,513 differentially expressed genes (4,769 upregulated and 4,744 downregulated genes; false discovery rate <0.05), including the positive expression of the Mφ-specific markers *CD68*, *Lgals3*, *Marco*, and *MerTK*. The classical activated Mφ signaling pathway was identified as one of the enriched canonical pathways by Ingenuity Pathway Analysis (IPA) with a *Z* score of −4.23 (Figure 5C), suggesting substantial loss of the M1 signature in PGE$_2$-treated Mφ. Conversely, PGE$_2$-treated Mφ under hypoxic conditions exhibited marked upregulation of *Arg1*, *Ym1*, *Ym2*, *Fizz-1*, *Vegfa*, *Pparg*, and *CD206*, thus displaying a gene profile most indicative of the M2a subtype over M2b, M2c, and M2d subtypes (Figure S5D). Since M2a-φ are key mediators of wound healing through secretion of an array of potent paracrine factors,[41] PGE$_2$-treated M2φ showed induced protein expression of

vascular endothelial growth factor A (VEGF-A), and transforming growth factor β (TGF-β) (Figure 5D) documented EMT- and angiogenesis-inducing factors in breast tumors, respectively.[41] We next examined the pro-metastatic capacity of paracrine factors secreted from PGE$_2$-treated M2-like Mφ (Figure 5E). Incubation of Py230 cells with PGE$_2$ Mφ conditioned medium (MφCM) promoted more rapid migration than that of control MφCM (Figure 5F), concordant with the downregulation of E-cadherin and upregulation of N-cadherin independently shown in western blotting and immunofluorescent staining (Figures 5G and 5H). Additionally, tube-formation capacity was significantly higher when bEnd.3 mouse endothelial cells were incubated with PGE$_2$ MφCM (Figure 5I). Consistently, ELISA assays showed higher levels of VEGF-A and TGF-β1 protein in the tumor interstitial fluids of biopsied tumors compared to unbiopsied controls (Figure 5J). Lastly, IHC validated local induction of both VEGF and TGF-β1 adjacent to the biopsy wound (Figure S5E), consistently supporting M2φ-derived paracrine factors as mediator of pro-metastatic changes in the biopsy wound.

PGE$_2$ induces M2 shift via the EP2 receptor

PGE$_2$ exerts its action through four integral membranous prostanoid receptors (EP1–EP4) that are ubiquitously expressed,[46] including in bone marrow-derived primary Mφ (Figure S6A). To identify the prostanoid receptor that mediates PGE$_2$-induced M2 shift under hypoxic conditions, Mφ were preincubated with selective pharmacologic EP1–EP4 inhibitors for 1 h before exposure to PGE$_2$ for 24 h. EP2 inhibitor (PF04418948) abolished PGE$_2$-induced *Arg1* mRNA expression, whereas no inhibitory effect was noted with antagonists against receptors EP1 (ONO8711), EP3 (L-798106), or EP4 (GW-627368X) (Figure 6A). Conversely, EP2 agonists (CP-544326) mimicked PGE$_2$-induced *Arg1* mRNA expression, while agonists for EP1/EP3 (17-phenyl trinor PGE$_2$) and EP4 (ONO-4819) did not (Figure 6B). Of note, the viability of Mφ was unaffected after 24 h of incubation with these compounds (Figure S6B). Consistent with pharmacologic inhibition, genetic ablation of *Ep2* in Mφ isolated from the femur bone of female *Ep2$^{−/−}$* mice abrogated PGE$_2$-induced *Arg1* mRNA expression (Figure 6C), while *Ep2$^{−/−}$* Mφ retained the capacity to undergo interleukin-4-induced M2 shift (Figure S6C). Interestingly, PGE$_2$ upregulated *Ep2* mRNA levels under hypoxic conditions (Figure 6D). Accordingly, PGE$_2$-induced expression of VEGF and TGF-β1 in *Ep2$^{+/+}$* subsided in *Ep2$^{−/−}$* Mφ (Figure 6E).

(B) RT-qPCR analysis of *Arg1* mRNA expression in the primary Mφ treated with or without PGE$_2$ under normoxia (n = 4) or hypoxia (n = 8) and normalized by *Gapdh*. The data are shown as standard boxplots; p values were calculated using Student's t test.

(C) Transcript expression analysis of IPA-selected classically activated Mφ (M1φ) in B6 control Mφ vs. PGE$_2$-treated Mφ for 24 h under hypoxia (n = 3).

(D) Immunofluorescence (IF) images of VEGF and TGF-β1 of Mφ treated with or without PGE$_2$ under hypoxia (n = 4).

(E) Schematic diagram of experimental flow of *in vitro* assays. Py230 and bEnd.3 cells were treated with conditioned medium (CM) collected from Mφ treated with PGE$_2$.

(F) Wound-healing assay graph depicts the remaining areas after 12 h incubation, relative to untreated control (n = 9). p values were calculated using Student's t test. The data are shown as mean ± SEM.

(G) IF images indicate Py230 cells treated with CM for 16 h (n = 4).

(H) Expression of E- and N-cadherin normalized by GAPDH (n = 5) in Py230 cells treated with MφCM for 16 h analyzed by western blot were compared using Student's t test. The data are shown as mean ± SEM.

(I) Tube-formation assay of bEnd.3 cells treated with MφCM for 8 h (n = 3) were compared by Student's t test. The data are shown as mean ± SEM.

(J) ELISA assays for TGF-β1 and VEGF-A of interstitial fluids collected from biopsied or unbiopsied Py230 tumors (n = 4) were calculated using Student's t test. The data are shown as mean ± SEM.
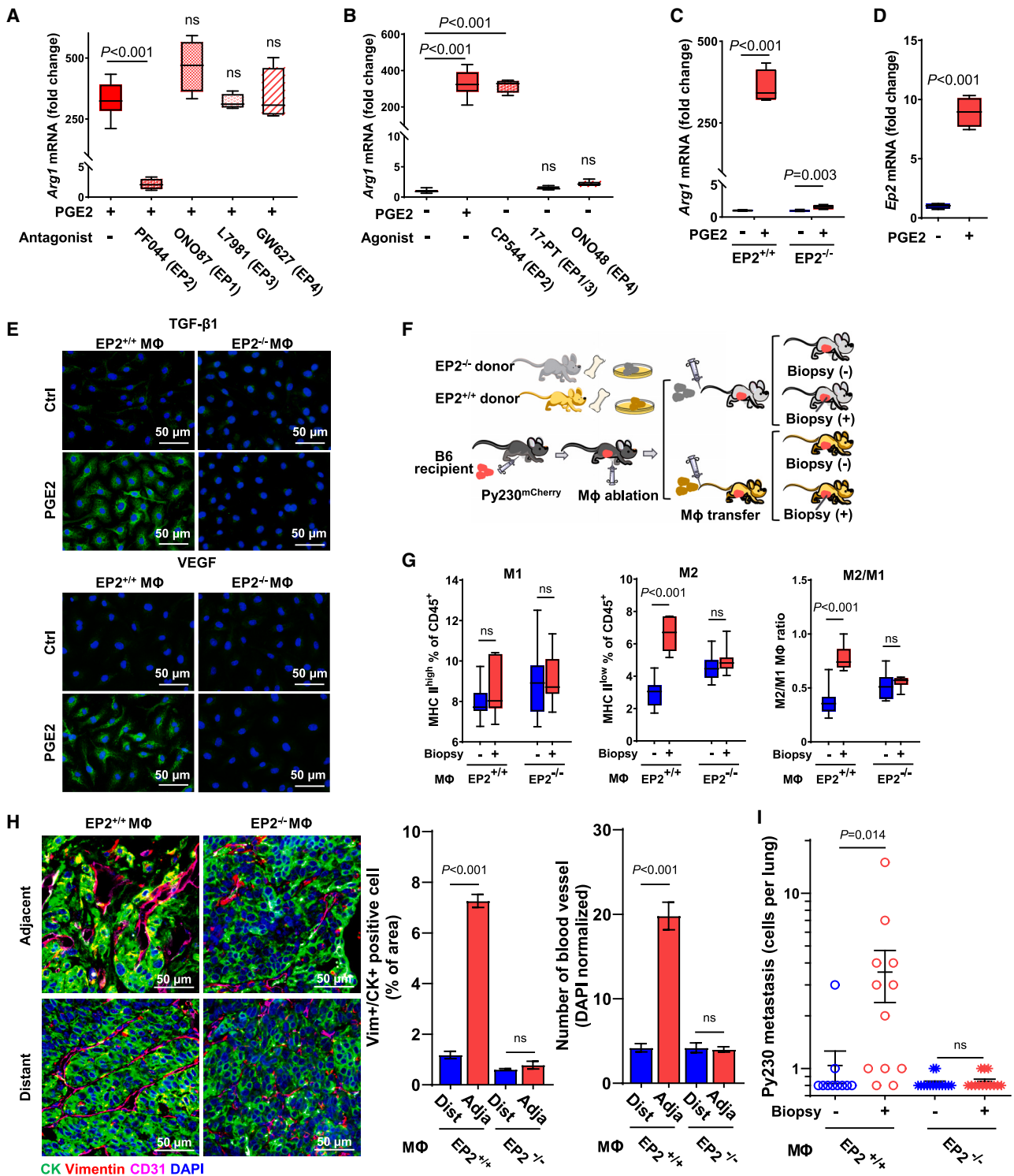
Figure 6. PGE$_2$/EP2 axis is the driver of biopsy-induced M2 polarization, EMT, and systemic dissemination

(A) RT-qPCR analysis of *Arg1* mRNA expression in the primary MΦ co-treated with PGE$_2$ and antagonists for EP1 (10 nM, ONO8711), EP2 (1 μM, PF04418948), EP3 (10 nM, L-798106), or EP4 (1 μM, GW-627368X). Relative expression was compared between five treatment groups using one-way ANOVA, relative to PGE$_2$ treatment (n = 4–8). The data are shown as standard boxplots.

(B) MΦ treated with EP receptor agonist for EP1 + EP3 (1 μM, 17PT PGE$_2$), EP2 (150 nM, CP544326), or EP4 (100 nM, ONO-4819) for *Arg1* mRNA expression was compared using one-way ANOVA, relative to control (n = 4). The data are shown as standard boxplots.

To further validate the role of EP2 in infiltrating Mφ in biopsy-induced pro-metastatic progression *in vivo*, immunophenotypic profiling was performed following adoptive transfer of either *Ep2*$^{+/+}$ or *Ep2*$^{-/-}$ Mφ (Figure 6F). The biopsy-induced M2φ shift was disrupted in mice that received adoptive transfer of *Ep2*$^{-/-}$ Mφ, without notable differences detected in M1φ and M2φ fractions in *Ep2*$^{-/-}$ Mφ recipients regardless of biopsy status (Figure 6G). In contrast, biopsy-induced M2φ shift remained intact in *Ep2*$^{+/+}$ Mφ recipients. Additionally, vimentin$^+$/CK$^+$ cancer cells were rarely detected adjacent to the biopsy wounds of Py230 tumors in *Ep2*$^{-/-}$ Mφ recipients, relative to their prevalence in biopsied tumors from *Ep2*$^{+/+}$ Mφ recipient mice (Figure 6H). Similarly, the substantial increase in CD31$^+$ blood vessels adjacent to the biopsy wound detected in *Ep2*$^{+/+}$ Mφ recipients was absent in *Ep2*$^{-/-}$ Mφ recipients (Figure 6H). Lastly, biopsy-induced systemic dissemination of Py230^{mCherry} cells to the lungs observed in *Ep2*$^{+/+}$ Mφ recipient mice was completely abrogated in *Ep2*$^{-/-}$ Mφ recipients (Figure 6I). Thus, these pharmacologic and genetic data support a critical role of the PGE$_2$/EP2 axis in infiltrating Mφ on biopsy-induced M2φ dominance and the associated features of EMT, angiogenesis, and systemic cancer cell dissemination.

Pharmacologic inhibition of COX-2 or EP2 suppresses biopsy-induced systemic dissemination of cancer cells

Given the critical role of the COX-2/PGE$_2$/EP2 feedforward loop on a series of biopsy-induced pro-metastatic effects, we postulated that oral administration of selective inhibitors of COX-2 (celecoxib) or EP2 (PF04418948) would alleviate biopsy-induced pro-metastatic changes. Py230^{mCherry} tumor-bearing mice were biopsied and then fed a dough diet containing celecoxib, PF04418948, or corn oil (vehicle) *ad libitum* starting 24 h after the biopsy. Oral celecoxib or PF04418948 significantly reduced the number of metastatic Py230 cells in the lung to a level similar to that of mice with unbiopsied tumors (Figure 7A). Neither celecoxib nor PF04418948, at the dose used in this study, had a detectable inhibitory effect on basal levels of cancer cell dissemination as well as tumor growth (Figures 7A and S7A). IHC staining of tumors revealed significant reductions in biopsy-induced CD206$^+$ M2-like Mφ, F4/80$^+$ Mφ, TGF-β1, and VEGF densities around the biopsy wounds in celecoxib- and PF04418948-treated mice (Figures 7B and S7B). Interestingly, celecoxib- or

PF04418948-treated mice showed biopsy wounds with well-differentiated epithelial borders and fewer residual inflammatory cells, as opposed to the high-cellularity wound stroma of biopsied tumors from vehicle-treated mice (Figure S7B), suggesting that blockade of the COX-2/PGE$_2$/EP2 feedforward loop alleviates the observed delayed healing of tumor biopsy wounds. Subsequently, PF04418948 and celecoxib treatment significantly inhibited biopsy-induced cancer cell EMT as evidenced by reductions in vimentin$^+$/CK$^+$ and increases in E-cadherin$^+$/CK$^+$ proportions (Figures 7C and 7D).

A model summarizing the proposed mechanisms underlying biopsy-induced pro-metastatic progression of breast tumors is presented in Figure 7E. Needle biopsy of the tumor leaves a metastasis-permissive unhealed wound that features continuous activation of COX-2/PGE$_2$ in the infiltrating stromal cells, which synergistically favors EP2-dependent M2 shift of infiltrating Mφ in the hypoxic biopsy wound. In turn, M2φ-secreted paracrine factors, including TGF-β1 and VEGF, promote EMT of nearby cancer cells and local angiogenesis. The biopsy-induced development of such a metastasis-permissive milieu substantially elevates the basal rate of systemic dissemination of cancer cells, thus increasing the risk for the establishment of clinically relevant distant metastases, which may, in part, provide a biological explanation for the accelerated mortality risk associated with the biopsy-to-surgery interval. Oral administration of selective inhibitors of COX-2 or EP2 after biopsy may prevent biopsy-induced pro-metastatic alterations within tumors and subsequent systemic cancer cell dissemination. Thus, surgery within a 53-day safety window or pharmacologic blockade of the COX-2/PGE$_2$/EP2 feedforward loop mitigates biopsy-induced metastasis.

DISCUSSION

Through a multi-disciplinary approach, the current study provided coherent evidence that needle biopsy of ER$^+$ BC leaves a wound stroma that enhances progressive pro-metastatic changes conducive to systemic dissemination of cancer cells. Our cohort analysis provided the conceptual framework for biopsy-induced pro-metastatic progression by delineating a biphasic trajectory with delayed onset of mortality-risk increase when the biopsy-to-surgery interval exceeds approximately

(C) *Arg1* mRNA expression in *Ep2*$^{+/+}$ Mφ and *Ep2*$^{-/-}$ Mφ treated with or without PGE$_2$ (n = 4) was compared using two-way ANOVA, relative to control. The data are shown as standard boxplots.

(D) *Ep2* mRNA expression in Mφ treated with or without PGE$_2$ under hypoxia (n = 4) was compared using Student's t test. The data are shown as standard boxplots.

(E) IF images of VEGF and TGF-β1 of *Ep2*$^{+/+}$ Mφ and *Ep2*$^{-/-}$ Mφ treated with or without PGE$_2$ under hypoxia (n = 4).

(F) Schematic diagram of experimental flow of Mφ adoptive transfer. Py230 tumor-bearing recipient mice were treated with clodronate once for Mφ depletion and then received adoptive transfer of Mφ isolated from *Ep2*$^{+/+}$ or *Ep2*$^{-/-}$ donor mice, after which they received biopsy or were left unbiopsied. Tumors were isolated 15 days after the biopsy.

(G) Immunoprofiling of Mφ isolated from Py230 tumors of *Ep2*$^{+/+}$ Mφ or *Ep2*$^{-/-}$ Mφ recipients (n = 7). The data are shown as standard boxplots; p values were calculated using two-way ANOVA, relative to the unbiopsied control.

(H) Representative images of two distinct areas adjacent to or distant from biopsy wound in 15-day post-biopsy Py230 tumors, immunofluorescently stained for CD31 (pink), CK (green), and vimentin (red), and counterstained with DAPI (blue). Graph summarizes the percentage of vimentin$^+$/CK$^+$ cells and CD31$^+$ blood vessel count, normalized by nucleus count per field of view at the final magnification of 40× (n = 5). The data are shown as mean ± SEM; p values were calculated using two-way ANOVA, relative to distant.

(I) Graph depicting the number of metastatic Py230^{mCherry} cells in the lung of *Ep2*$^{+/+}$ Mφ or *Ep2*$^{-/-}$ Mφ recipient mice that were biopsied or unbiopsied (n = 10–14). Data were plotted as means ± SEM; p values were calculated using two-way ANOVA, relative to the unbiopsied control.
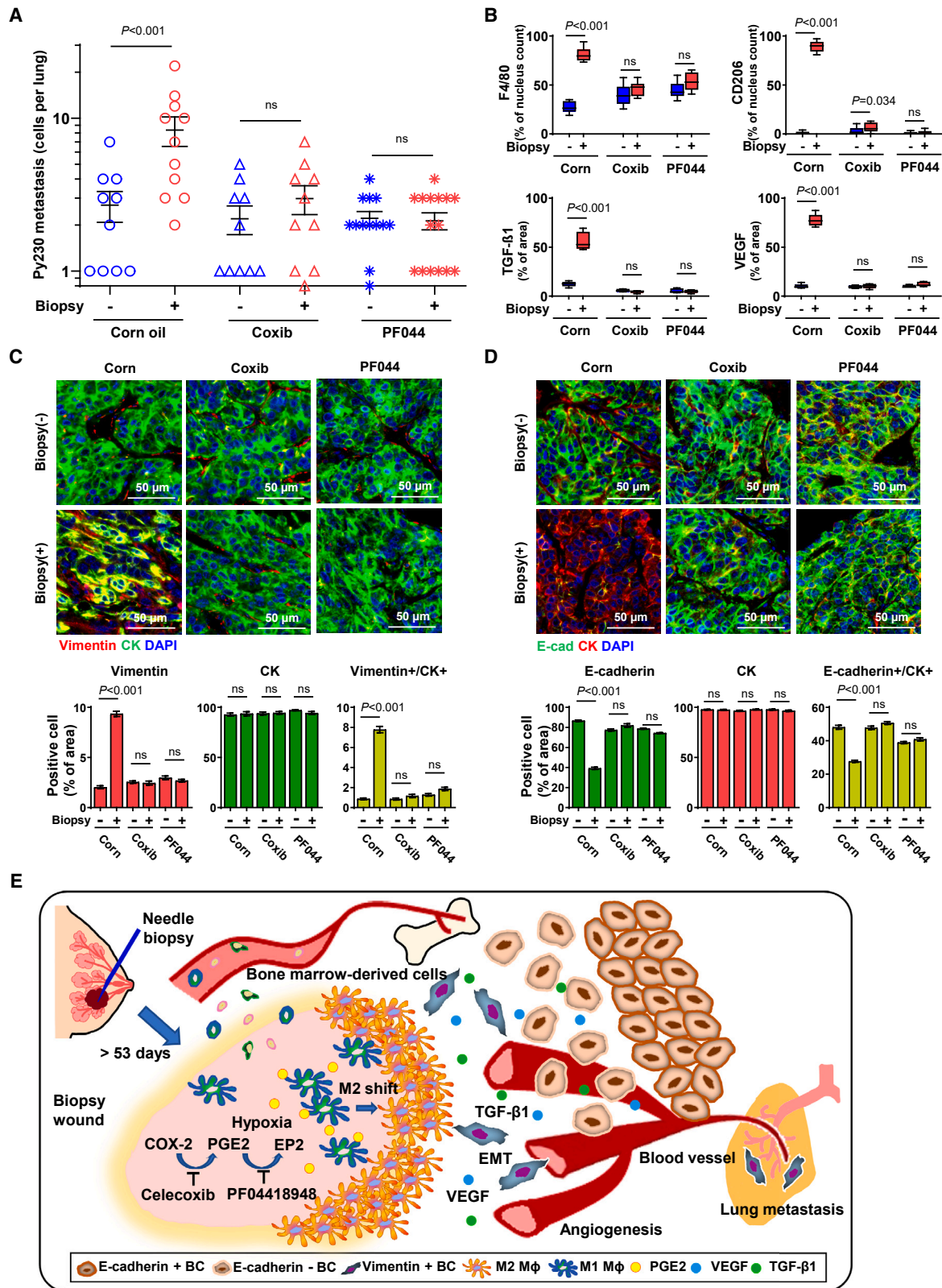
two months. Multiplex immunofluorescence analyses of human and mouse breast tumors supported biopsy-induced pro-metastatic changes, with increased levels of mesenchymal-like BC cells and angiogenesis detected adjacent to the M2φ-dominated biopsy wound stroma. Preclinical mouse tumor models and *in vitro* experiments supported the notion that continuous activation of the COX-2/PGE$_2$/EP2 feedforward loop in infiltrating stromal cells of the biopsied tumor promoted M2-like Mφ dominance that enhances EMT and systemic dissemination of cancer cells. Lastly, the prevention of biopsy-induced pro-metastatic progression in preclinical models via oral administration of selective inhibitors for COX-2 and EP2 provides a pharmacologic strategy for clinical management to avoid excess mortality risk due to biopsy-induced pro-metastatic changes. Collectively, these observations counter the prevailing view that needle biopsy is safe in all settings, instead suggesting that pro-metastatic risk is associated with prolonged retention of the biopsy wound within malignant breast tumors.

Our approach of modeling mortality risk by continuous biopsy-to-surgery interval uncovered a delayed onset of accelerated mortality risk following diagnostic biopsy among early-stage BC patients. An unanswered question has been whether the natural disease progression of early-stage BC occurs in 60 days or disease progression is accelerated once diagnosed. For BC dissemination, at least two main routes have been suggested: linear progression that requires a series of pro-metastatic changes such as EMT or parallel progression through which inherently aggressive BC cells spread early after a pro-angiogenic switch kicks in.[47,48] Coupled with experimentally correlated evidence of long-lasting biopsy-wound-induced cellular and molecular alterations with the emergence of a 200- to 250-μm-deep EMT zone directly outside the pro-metastatic M2φ layers, our cohort data suggest that the mortality increase associated with prolonged biopsy-to-surgery interval underlies accelerated progression. It is important to note that our data neither dispute nor discourage diagnostic needle biopsy for BC; the biphasic mortality trajectory, featuring a period of no excess mortality-risk gain during the first 53 days post biopsy, rather emphasizes the safety of needle biopsy within this critical time window.

For successful systemic dissemination, a capacity for local invasion within the primary tumor is prerequisite.[35,49] Early onset of phenotypic transitions, EMT, and elevated expression of basal markers CK14 and CK17 were unexpected, based on the indolent nature of ER$^+$ BC.[50] Notably, it was reported that CK14$^+$ cells lead collective invasion of BC, imposing migration of CK14$^-$ cells

specifically in luminal A/B but not in triple-negative BC.[51] In this regard, ER$^+$ BC may be more permissive to the induction of phenotypic transition; the proposed mechanism of biopsy-induced metastasis, in which acquisition of migratory capacity via EMT is the driver of disease dissemination, may be applicable primarily to epithelial-like BC with a larger capacity for further phenotypic transition, but less to intrinsically mesenchymal-like tumors. Indeed, biopsy-induced metastasis reported in 4T1 mesenchymal-like triple-negative BC tumors is related to acute events, such as cell displacement or acute inflammation.[52,53] Additionally, based on the clinical management of ER$^-$ disease, the impact of needle biopsy may be better evaluated in the neoadjuvant setting.

COX-2 mediates pro-inflammatory responses in the wound-healing cascade[42]; protracted COX-2 activity is reported in an unhealed wound as commonly seen in individuals with diabetes.[54] Intriguingly, the concomitant presentation of opposite inflammatory responses in spatially distinctive wound compartments, an inner COX-2-active pro-inflammatory biopsy cavity encapsulated by an M2φ-predominant anti-inflammatory layer, signifies impaired healing of tumor biopsy wounds. Needle biopsy appears to introduce a biologically complex milieu, "acute-to-chronic wound within solid tumor," which may reciprocally stimulate tumor progression between wound and tumor.[55,56] In the hypoxic biopsy wound, PGE$_2$ released from infiltrating stromal cells indirectly provokes pro-metastatic changes by exerting M2 shift. PGE$_2$ also exerts direct pro-tumor effects through EP receptors of cancer cells[57]; possible congruent effects may act in concert and contribute to biopsy-induced cancer cell EMT and metastasis. Another example of such is unresolved hypoxia. Hypoxia not only causes impaired wound healing but also tumor progression; a myriad of biological factors pertinent to both may be skewed, including, but not limited to, altered signaling of cancer cells,[58] likely crosstalk with other infiltrating stromal cells or with cancer cells,[59] and Mφ recruitment and their longevity.[60] Further in-depth characterization of the causal factors of protracted COX-2 and M2-like Mφ abundance is expected to provide a more comprehensive understanding of biopsy-induced tumor progression of BC.

Currently, non-steroidal anti-inflammatory drugs (NSAIDs) are not recommended after biopsy due to their anti-coagulation effect; however, selective NSAIDs with no anti-coagulation potential may be repurposed for the prevention of biopsy-induced pro-metastatic progression in patients for whom a longer biopsy-to-surgery interval may offer clinical merit.[18,61–63] While this study adopted anti-inflammatory doses for oral

Figure 7. Oral administration of COX-2- or EP2-selective inhibitors prevented biopsy-induced pro-metastatic changes and systemic dissemination of cancer cells

(A) Py230^{mCherry} tumor-bearing recipient mice were orally administered corn oil control (n = 10–11), celecoxib (n = 10), or PF04418948 (n = 13–15) in food *ad libitum* from day 2 to day 15 (n = 10–15). The graph depicts the number of metastatic Py230^{mCherry} cells in the lung. The data are shown as mean ± SEM; p values were calculated using two-way ANOVA, relative to the unbiopsied control.

(B) Graphs depicting the IHC-measured F4/80 and CD206 densities normalized by nucleus count per field of view at a final magnification of 40×. The intensity of VEGF and TGF-β1 was normalized by area at a final magnification of 40×. The data are shown as standard boxplots; p values were calculated using two-way ANOVA, relative to unbiopsied control (n = 10–15).

(C and D) Representative images of 15-day post-biopsy Py230 tumors immunofluorescently stained for (C) vimentin (red), CK (green), and DAPI (blue) or (D) CK (red), E-cadherin (green), and DAPI (blue). Pixels were normalized by nucleus count per field of view at a final magnification of 40× (n = 10–12). Data were plotted as mean ± SEM; p values were calculated using two-way ANOVA, relative to unbiopsied control.

(E) Illustrated working hypothesis of biopsy-induced metastasis and pharmacologic prevention.

administration, the type, duration, timing of initiation, dose, and dose rate for prophylactic use of NSAIDs during the biopsy-to-surgery interval should be further investigated in a randomized clinical study.

In conclusion, needle biopsy of early-stage ER$^+$ BC instigates rapid pro-metastatic progression, which likely explains, at least in part, the increased mortality risk detected among patients who receive therapeutic surgery approximately two or more months after diagnostic biopsy. Thus, our data support the recent recommendation of keeping the diagnosis-to-surgery time within 60 days or fewer and provides a rationale for a pharmacologic strategy to inhibit the COX-2/PGE$_2$/EP2 feedforward loop in cases where delay of surgery is unavoidable.

Limitations of the study

One of the clinical issues in the management of localized BC, especially ER$^+$ disease, is a life-long risk of recurrence from latent or dormant metastatic cells at distant sites.[3,4] Because the elevated and continuous mortality risk posed by surgery delay may be attributable to an increased burden of latent tumor cells (Figures 1B and 1C), we chose early disease dissemination in the lungs as the endpoint in response to biopsy in two independent low-metastatic mouse models. While the experimental models supported the concept of biopsy-induced metastatic dissemination of cancer cells, future studies are needed to determine whether disseminated cancer cells will progress to overt metastases under the standard of care of adjuvant endocrine therapy. In addition, the emergence of EMT along with M2-like Mφ around the biopsy wound in patient tumors (Figures 2C and 3C) corroborated the pro-metastatic changes associated with needle biopsy. However, due to a limited sample size, the current study lacks statistical evidence of whether the pro-metastatic histologic changes in the biopsy wound are associated with recurrence or mortality in patients with surgery delay. Further studies are needed to establish the association between mortality and biopsy-associated pro-metastatic histologic alterations in tumors from larger patient cohorts that include different intervals from biopsy to surgery (e.g., timely surgery vs. delayed surgery).

STAR★METHODS

Detailed methods are provided in the online version of this paper and include the following:

- **KEY RESOURCES TABLE**
- **RESOURCE AVAILABILITY**
  - Lead contact
  - Materials availability
  - Data and code availability
- **EXPERIMENTAL MODEL AND STUDY PARTICIPANT DETAILS**
  - Human cohort
  - Cell culture
  - Breast tumor mouse models
- **METHOD DETAILS**
  - Whole bone marrow adoptive transfer for *in vivo* COX-2 promoter assay

- Mφ adoptive transfer
- *In vivo* hypoxia assay
- Immunohistochemistry
- Multiplex immunofluorescent imaging for clinical cases
- Immunofluorescence of cultured cells
- Multicolor flow cytometry for Mφ immunoprofile
- qRT-PCR of Mφ
- Illumina RNA-seq libraries
- Western blotting
- ELISA
- Would healing assay
- Tube formation assay
- **QUANTIFICATION AND STATISTICAL ANALYSIS**

AUTHOR CONTRIBUTIONS

T.T., H.R., and I.C. conceptualized the study and acquired funding. M.L., I.C., and R.P. performed cohort studies. M.L., I.C., T.T., and H.R. contributed to interpretation of the cohort study. H.K. performed all mouse studies and *in vitro* assays. R.S., J.F.L., and Y.S. performed multiplex IHC of mice and human breast tumors. H.K., J.F.L., Y.S., A.R., and S.N. performed quantitative analysis of IHC data. K.-M.F. provided patient samples. P.D. performed western blotting and PCR. S.-W.T. performed the bioinformatics of RNA-sequencing data. I.C. and M.Y. performed statistical analyses. H.K., T.T., I.C., and H.R. interpreted data derived from the mouse experiments. T.T., H.R., and I.C. supervised and wrote the manuscript. All authors reviewed and edited the manuscript.

REFERENCES

1. Siegel, R.L., Miller, K.D., Fuchs, H.E., and Jemal, A. (2022). Cancer statistics, 2022. CA A Cancer J. Clin. *72*, 7–33.

2. American College of Surgeons (2022). Stage of Breast Cancer Diagnosed in 2011 to 2020. https://reportsncdb.facs.org/BMPub/BMR_report_1st2.cfm?CFID=52910&CFTOKEN=a2896298027ffac5-D22B1D08-AD0A-CB86-01584285B4C806AD.

3. Early Breast Cancer Trialists' Collaborative Group EBCTCG; Davies, C., Godwin, J., Gray, R., Clarke, M., Cutter, D., Darby, S., McGale, P., Pan, H.C., Taylor, C., et al. (2011). Relevance of breast cancer hormone

receptors and other factors to the efficacy of adjuvant tamoxifen: patient-level meta-analysis of randomised trials. Lancet *378*, 771–784.

4. Pan, H., Gray, R., Braybrooke, J., Davies, C., Taylor, C., McGale, P., Peto, R., Pritchard, K.I., Bergh, J., Dowsett, M., et al. (2017). 20-Year Risks of Breast-Cancer Recurrence after Stopping Endocrine Therapy at 5 Years. N. Engl. J. Med. *377*, 1836–1846.

5. Hanna, T.P., King, W.D., Thibodeau, S., Jalink, M., Paulin, G.A., Harvey-Jones, E., O'Sullivan, D.E., Booth, C.M., Sullivan, R., and Aggarwal, A. (2020). Mortality due to cancer treatment delay: systematic review and meta-analysis. BMJ *371*, m4087.

6. Hills, N., Leslie, M., Davis, R., Crowell, M., Kameyama, H., Rui, H., Chervoneva, I., Dooley, W., and Tanaka, T. (2021). Prolonged Time from Diagnosis to Breast-Conserving Surgery is Associated with Upstaging in Hormone Receptor-Positive Invasive Ductal Breast Carcinoma. Ann. Surg Oncol. *28*, 5895–5905.

7. Bleicher, R.J., Ruth, K., Sigurdson, E.R., Beck, J.R., Ross, E., Wong, Y.N., Patel, S.A., Boraas, M., Chang, E.I., Topham, N.S., and Egleston, B.L. (2016). Time to Surgery and Breast Cancer Survival in the United States. JAMA Oncol. *2*, 330–339.

8. Bleicher, R.J., Ciocca, R.M., Egleston, B.L., Sesa, L., Evers, K., Sigurdson, E.R., and Morrow, M. (2009). Association of routine pretreatment magnetic resonance imaging with time to surgery, mastectomy rate, and margin status. J. Am. Coll. Surg. *209*, 180–187. quiz 294-185.

9. Eriksson, L., Bergh, J., Humphreys, K., Wärnberg, F., Törnberg, S., and Czene, K. (2018). Time from breast cancer diagnosis to therapeutic surgery and breast cancer prognosis: A population-based cohort study. Int. J. Cancer *143*, 1093–1104.

10. Mateo, A.M., Mazor, A.M., Obeid, E., Daly, J.M., Sigurdson, E.R., Handorf, E.A., DeMora, L., Aggon, A.A., and Bleicher, R.J. (2020). Time to Surgery and the Impact of Delay in the Non-Neoadjuvant Setting on Triple-Negative Breast Cancers and Other Phenotypes. Ann. Surg Oncol. *27*, 1679–1692.

11. The American College of Surgeons (2022). NCDB Announces New Breast Quality Measure.

12. Ghosh, K., Melton, L.J., 3rd, Suman, V.J., Grant, C.S., Sterioff, S., Brandt, K.R., Branch, C., Sellers, T.A., and Hartmann, L.C. (2005). Breast biopsy utilization: a population-based study. Arch. Intern. Med. *165*, 1593–1598.

13. Nassar, A. (2011). Core needle biopsy versus fine needle aspiration biopsy in breast–a historical perspective and opportunities in the modern era. Diagn. Cytopathol. *39*, 380–388.

14. Bulte, J.P., Simsek, D., Bult, P., de Wilt, J.H.W., and Strobbe, L.J.A. (2020). Trends in pre-operative needle biopsy use in invasive breast cancer diagnosis: a Dutch nationwide population study. Acta Oncol. *59*, 1469–1473.

15. Bertario, L., Reduzzi, D., Piromalli, D., Piva, L., and Di Pietro, S. (1985). Outpatient biopsy of breast cancer. Influence on survival. Ann. Surg. *201*, 64–67.

16. Abramson, D.J. (1966). 857 breast biopsies as an outpatient procedure: delayed mastectomy in 41 malignant cases. Ann. Surg. *163*, 478–483.

17. Bilimoria, K.Y., Ko, C.Y., Tomlinson, J.S., Stewart, A.K., Talamonti, M.S., Hynes, D.L., Winchester, D.P., and Bentrem, D.J. (2011). Wait times for cancer surgery in the United States: trends and predictors of delays. Ann. Surg. *253*, 779–785.

18. Hulvat, M., Sandalow, N., Rademaker, A., Helenowski, I., and Hansen, N.M. (2010). Time from diagnosis to definitive operative treatment of operable breast cancer in the era of multimodal imaging. Surgery *148*, 746–750.

19. Paradiso, A., Lorusso, V., Tommasi, S., Schittulli, F., Maiello, E., and De Lena, M. (1988). Relevance of cell kinetics to hormonal response of receptor-positive advanced breast cancer. Breast Cancer Res. Treat. *11*, 31–36.

20. Paradiso, A., Tommasi, S., Mangia, A., Lorusso, V., Simone, G., and De Lena, M. (1990). Tumor-proliferative activity, progesterone receptor status, estrogen receptor level, and clinical outcome of estrogen receptor-positive advanced breast cancer. Cancer Res. *50*, 2958–2962.

21. Gobbi, H., Tse, G., Page, D.L., Olson, S.J., Jensen, R.A., and Simpson, J.F. (2000). Reactive spindle cell nodules of the breast after core biopsy or fine-needle aspiration. Am. J. Clin. Pathol. *113*, 288–294.

22. Hoorntje, L.E., Schipper, M.E.I., Kaya, A., Verkooijen, H.M., Klinkenbijl, J.G., and Borel Rinkes, I.H.M. (2004). Tumour cell displacement after 14G breast biopsy. Eur. J. Surg. Oncol. *30*, 520–525.

23. Layfield, L.J., Frazier, S., and Schanzmeyer, E. (2015). Histomorphologic Features of Biopsy Sites Following Excisional and Core Needle Biopsies of the Breast. Breast J. *21*, 370–376.

24. McCarty, C., Yi, M., Sous, S., Leslie, M., Tariq, E., Dondapati, P., Kameyama, H., Nuguri, S., Hills, N., Wilkerson, M., et al. (2023). Sustained Inflammation of Breast Tumors after Needle Biopsy. Pathobiology *90*, 114–122.

25. Koh, T.J., and DiPietro, L.A. (2011). Inflammation and wound healing: the role of the macrophage. Expet Rev. Mol. Med. *13*, e23.

26. MacCarthy-Morrogh, L., and Martin, P. (2020). The hallmarks of cancer are also the hallmarks of wound healing. Sci. Signal. *13*, eaay8690.

27. Rodrigues, M., Kosaric, N., Bonham, C.A., and Gurtner, G.C. (2019). Wound Healing: A Cellular Perspective. Physiol. Rev. *99*, 665–706.

28. Minutti, C.M., Knipper, J.A., Allen, J.E., and Zaiss, D.M.W. (2017). Tissue-specific contribution of macrophages to wound healing. Semin. Cell Dev. Biol. *61*, 3–11.

29. Halpern, M.T., and Schrag, D. (2016). Effects of state-level medicaid policies and patient characteristics on time to breast cancer surgery among medicaid beneficiaries. Breast Cancer Res. Treat. *158*, 573–581.

30. Lambert, A.W., Pattabiraman, D.R., and Weinberg, R.A. (2017). Emerging Biological Principles of Metastasis. Cell *168*, 670–691.

31. Thiery, J.P. (2002). Epithelial-mesenchymal transitions in tumour progression. Nat. Rev. Cancer *2*, 442–454.

32. Kalluri, R. (2009). EMT: when epithelial cells decide to become mesenchymal-like cells. J. Clin. Invest. *119*, 1417–1419.

33. Abd El-Rehim, D.M., Pinder, S.E., Paish, C.E., Bell, J., Blamey, R.W., Robertson, J.F.R., Nicholson, R.I., and Ellis, I.O. (2004). Expression of luminal and basal cytokeratins in human breast carcinoma. J. Pathol. *203*, 661–671.

34. McGinn, O., Riley, D., Finlay-Schultz, J., Paul, K.V., Kabos, P., and Sartorius, C.A. (2022). Cytokeratins 5 and 17 maintain an aggressive epithelial state in basal-like breast cancer. Mol. Cancer Res. *20*, 1443–1455. MCR-21-0866.

35. Yang, J., Antin, P., Berx, G., Blanpain, C., Brabletz, T., Bronner, M., Campbell, K., Cano, A., Casanova, J., Christofori, G., et al. (2020). Guidelines and definitions for research on epithelial-mesenchymal transition. Nat. Rev. Mol. Cell Biol. *21*, 341–352.

36. Rodero, M.P., Licata, F., Poupel, L., Hamon, P., Khosrotehrani, K., Combadiere, C., and Boissonnas, A. (2014). In vivo imaging reveals a pioneer wave of monocyte recruitment into mouse skin wounds. PLoS One *9*, e108212.

37. Yanez, D.A., Lacher, R.K., Vidyarthi, A., and Colegio, O.R. (2017). The role of macrophages in skin homeostasis. Pflügers Archiv *469*, 455–463.

38. Eming, S.A., Martin, P., and Tomic-Canic, M. (2014). Wound repair and regeneration: mechanisms, signaling, and translation. Sci. Transl. Med. *6*, 265sr6.

39. Vintersten, K., Monetti, C., Gertsenstein, M., Zhang, P., Laszlo, L., Biechele, S., and Nagy, A. (2004). Mouse in red: red fluorescent protein expression in mouse ES cells, embryos, and adult animals. Genesis *40*, 241–246.

40. Maisel, B.A., Yi, M., Peck, A.R., Sun, Y., Hooke, J.A., Kovatich, A.J., Shriver, C.D., Hu, H., Nevalainen, M.T., Tanaka, T., et al. (2022). Spatial Metrics of Interaction between CD163-Positive Macrophages and Cancer Cells and Progression-Free Survival in Chemo-Treated Breast Cancer. Cancers *14*, 308.

41. Forbes, S.J., and Rosenthal, N. (2014). Preparing the ground for tissue regeneration: from mechanism to therapy. Nat. Med. *20*, 857–869.

42. Smyth, E.M., Grosser, T., Wang, M., Yu, Y., and FitzGerald, G.A. (2009). Prostanoids in health and disease. J. Lipid Res. *50 (Suppl)*, S423–S428.

43. Ishikawa, T.O., Jain, N.K., Taketo, M.M., and Herschman, H.R. (2006). Imaging cyclooxygenase-2 (Cox-2) gene expression in living animals with a luciferase knock-in reporter gene. Mol. Imag. Biol. *8*, 171–187.

44. Rodriguez, P.G., Felix, F.N., Woodley, D.T., and Shim, E.K. (2008). The role of oxygen in wound healing: a review of the literature. Dermatol. Surg. *34*, 1159–1169.

45. Sano, H., Ichioka, S., and Sekiya, N. (2012). Influence of oxygen on wound healing dynamics: assessment in a novel wound mouse model under a variable oxygen environment. PLoS One *7*, e50212.

46. Harris, S.G., Padilla, J., Koumas, L., Ray, D., and Phipps, R.P. (2002). Prostaglandins as modulators of immunity. Trends Immunol. *23*, 144–150.

47. Gui, P., and Bivona, T.G. (2022). Evolution of metastasis: new tools and insights. Trends Cancer *8*, 98–109.

48. Klein, C.A. (2009). Parallel progression of primary tumours and metastases. Nat. Rev. Cancer *9*, 302–312.

49. Clark, A.G., and Vignjevic, D.M. (2015). Modes of cancer cell invasion and the role of the microenvironment. Curr. Opin. Cell Biol. *36*, 13–22.

50. McAndrew, N.P., and Finn, R.S. (2022). Clinical Review on the Management of Hormone Receptor-Positive Metastatic Breast Cancer. JCO Oncol. Pract. *18*, 319–327.

51. Cheung, K.J., Gabrielson, E., Werb, Z., and Ewald, A.J. (2013). Collective invasion in breast cancer requires a conserved basal epithelial program. Cell *155*, 1639–1651.

52. Hobson, J., Gummadidala, P., Silverstrim, B., Grier, D., Bunn, J., James, T., and Rincon, M. (2013). Acute inflammation induced by the biopsy of mouse mammary tumors promotes the development of metastasis. Breast Cancer Res. Treat. *139*, 391–401.

53. Mathenge, E.G., Dean, C.A., Clements, D., Vaghar-Kashani, A., Photopoulos, S., Coyle, K.M., Giacomantonio, M., Malueth, B., Nunokawa, A., Jordan, J., et al. (2014). Core needle biopsy of breast cancer tumors increases distant metastases in a mouse model. Neoplasia *16*, 950–960.

54. Pastar, I., Marjanovic, J., Stone, R.C., Chen, V., Burgess, J.L., Mervis, J.S., and Tomic-Canic, M. (2021). Epigenetic regulation of cellular functions in wound healing. Exp. Dermatol. *30*, 1073–1089.

55. Erler, J.T., Bennewith, K.L., Cox, T.R., Lang, G., Bird, D., Koong, A., Le, Q.T., and Giaccia, A.J. (2009). Hypoxia-induced lysyl oxidase is a critical mediator of bone marrow cell recruitment to form the premetastatic niche. Cancer Cell *15*, 35–44.

56. Stuelten, C.H., Barbul, A., Busch, J.I., Sutton, E., Katz, R., Sato, M., Wakefield, L.M., Roberts, A.B., and Niederhuber, J.E. (2008). Acute wounds accelerate tumorigenesis by a T cell-dependent mechanism. Cancer Res. *68*, 7278–7282.

57. Ma, X., Kundu, N., Collin, P.D., Goloubeva, O., and Fulton, A.M. (2012). Frondoside A inhibits breast cancer metastasis and antagonizes prostaglandin E receptors EP4 and EP2. Breast Cancer Res. Treat. *132*, 1001–1008.

58. Gilkes, D.M., Semenza, G.L., and Wirtz, D. (2014). Hypoxia and the extracellular matrix: drivers of tumour metastasis. Nat. Rev. Cancer *14*, 430–439.

59. Bai, R., Li, Y., Jian, L., Yang, Y., Zhao, L., and Wei, M. (2022). The hypoxia-driven crosstalk between tumor and tumor-associated macrophages: mechanisms and clinical treatment strategies. Mol. Cancer *21*, 177.

60. Lin, N., and Simon, M.C. (2016). Hypoxia-inducible factors: key regulators of myeloid cells during inflammation. J. Clin. Invest. *126*, 3661–3671.

61. Kurian, A.W., Li, Y., Hamilton, A.S., Ward, K.C., Hawley, S.T., Morrow, M., McLeod, M.C., Jagsi, R., and Katz, S.J. (2017). Gaps in Incorporating Germline Genetic Testing Into Treatment Decision-Making for Early-Stage Breast Cancer. J. Clin. Oncol. *35*, 2232–2239.

62. Greer, A.C., Lanes, A., Poorvu, P.D., Kennedy, P., Thomas, A.M., Partridge, A.H., and Ginsburg, E.S. (2021). The impact of fertility preservation on the timing of breast cancer treatment, recurrence, and survival. Cancer *127*, 3872–3880.

63. Bleicher, R.J., Ruth, K., Sigurdson, E.R., Ross, E., Wong, Y.N., Patel, S.A., Boraas, M., Topham, N.S., and Egleston, B.L. (2012). Preoperative delays in the US Medicare population with breast cancer. J. Clin. Oncol. *30*, 4485–4492.

STAR★METHODS

KEY RESOURCES TABLE

REAGENT or RESOURCE	SOURCE	IDENTIFIER
Antibodies		
CD163 (Human MIF)	Leica Biosystems	CD163-L-CE; RRID: AB_2920861
CD206 (Human MIF)	Abcam	Ab64693; RRID: AB_1523910
Pan-Cytokeratin (Human MIF)	Agilent	M3515; RRID: AB_2132885
E-cadherin (Human MIF)	Agilent	M3612; RRID: AB_2076672
E-cadherin (Mouse MIF)	Thermo Fisher Scientific	13–1900; RRID: AB_2533005
Vimentin (Mouse MIF)	Thermo Fisher Scientific	PA5-27231; RRID: AB_2544707
Pan-Cytokeratin (Mouse MIF)	Abcam	ab6401; RRID: AB_305450
Pan-Cytokeratin (Mouse MIF)	Dako	M3515; RRID: AB_2132885
AF488-CD206 (Mouse MIF)	Biolegend	141709; RRID: AB_10933252
COX-2 (Mouse MIF, IHC)	Abcam	ab15191; RRID: AB_2085144
MACH 2 Mouse HRP-Polymer (IHC)	Biocare Medical	MHRP520
MACH 2 Rabbit HRP-Polymer (IHC)	Biocare Medical	RHRP520
Rat-on-Mouse HRP-Polymer (IHC)	Biocare Medical	RT517
MACH 2 Rabbit AP-Polymer (IHC)	Biocare Medical	RALP525
mCherry (IHC-P)	Thermo Fisher Scientific	PA5-34974; RRID: AB_2552323
Pimonidazole (IHC-F)	Hypoxyprobe	HP1-100; RRID: AB_2811309
COX-2 (Human IHC)	Abcam	Ab15191; RRID: AB_2085144
Cytokeratin14 (IHC)	Biolegend	905303; RRID: AB_2734678
Cytokeratin17 (IHC)	Novus	NBP1-32824; RRID: AB_2133042
F4/80 (IHC)	Genetex	GTX26640; RRID: AB_385952
CD206 (IHC)	Abcam	ab64693; RRID: AB_1523910
VEGF (IHC)	Thermo Fisher Scientific	PA5-85171; RRID: AB_2792317
CD31 (MIF)	R&D Systems	AF3628; RRID: AB_2161028
TGF-β1 (IF)	MilliporeSigma	SAB4502954; RRID: AB_10747473
VEGF-A (IF)	Thermo Fisher Scientific	MA5-13182; RRID: AB_10981661
E-cadherin (IF, WB)	Thermo Fisher Scientific	13–1900; RRID: AB_2533005
N-cadherin (IF, WB)	BD Transduction Laboratories	610920; RRID: AB_2077527
Arginase-1 (WB)	Cell Signaling Technology	93668; RRID: AB_2800207
GAPDH (WB)	MilliporeSigma	G9545; RRID: AB_796208
Vimentin (WB)	BD Pharmingen	550513; RRID: AB_393716
E-cadherin (WB)	Biolegend	147306; RRID: AB_2563230
COX-1 (WB)	Cayman Chemical	160110; RRID: AB_10078135
COX-2 (WB)	Cell Signaling Technology	4842; RRID: AB_2084968
mPGES2 (WB)	Cayman Chemical	160145; RRID: AB_10894462
TGF-β1 (WB)	Bioss Antibodies	bs-0086R; RRID: AB_10856457
VEGF (WB)	Abcam	ab68334; RRID: AB_1925554
PE-CD45 (FACS, Compensation control)	Biolegend	103105; RRID: AB_312970
BV421-CD45 (FACS, Compensation control)	Biolegend	103133; RRID: AB_10899570
PE/Cy7-CD45 (FACS, Compensation control)	Biolegend	103113; RRID: AB_312978
AF647-CD45 (FACS, Compensation control)	Biolegend	103123; RRID: AB_493534
BV785-CD45 (FACS)	Biolegend	103149; RRID: AB_2564590
PE-F4/80 (FACS)	Biolegend	123109; RRID: AB_893498
BV421-CD11c (FACS)	Biolegend	117343; RRID: AB_2563099
FITC-CD11b (FACS)	Biolegend	101205; RRID: AB_312788

(Continued on next page)

Continued

REAGENT or RESOURCE	SOURCE	IDENTIFIER
PE/Cy7-CD11b (FACS)	Biolegend	101215; RRID: AB_312798
AF647-MHC class II (FACS)	Biolegend	107617; RRID: AB_493526
Bacterial and virus strains		
lentivirus for firefly luciferase with UBC promoter + IRES2-mCherry-IRES-puromycin	GeneCopoeia	LPP-hLUC-Lv247-050
Biological samples		
Clinical breast cancer cases	OUHSC Pathology Archive	N/A
Chemicals and recombinant proteins		
Matrigel GFR	Corning	356231
D-Luciferin	PerkinElmer	122799
Clodronate liposomes	Liposoma	CP-020
Celecoxib	Cayman Chemical	10008672
PF04418948	Cayman Chemical	15016
ONO8711	Cayman Chemical	14070
L798106	Santa Cruz Biotechnology	sc-204047
GW627368X	Cayman Chemical	10009162
CP544326	Cayman Chemical	22945
17-phenyl trinor Prostaglandin E2	Cayman Chemical	14810
ONO4819	Cayman Chemical	13618
Lipopolysaccharides	MilliporeSigma	L3012
IFN-γ	Tonbo Biosciences	21-8311-U020
Prostaglandin E2	Cayman Chemical	14010
Collagenase A	MilliporeSigma	10103586001
DNase I	MilliporeSigma	10104159001
Liberase	MilliporeSigma	05401119001
Indomethacin	MilliporeSigma	I7378
Protease inhibitor	MilliporeSigma	04-693-159-001
Pimonidazole	Hypoxyprobe	HP-100
Butylated Hydroxytoluene	Spectrum	B1196
Betazoid DAB Chromogen	Biocare Medical	BDB2004
Vulcan Fast Red Chromogen	Biocare Medical	FR805
Cytosine β-D-arabinofuranoside hydrochloride	MilliporeSigma	C6645
Critical commercial assays		
Mouse PGE2 ELISA	Cayman Chemical	514010
Mouse VEGF ELISA	RayBiotech	ELM-VEGF-1
Mouse Free Active TGF-β1 ELISA	Biolegend	437707
Hypoxisense 680	PerkinElmer	NEV11070
Deposited data		
RNA-sequence of mouse macrophage	This paper	SRA: PRJNA1031635
Experimental models: Cell lines		
Py230 murine breast cancer cell line	Gift from Dr. Lesley G. Ellies (University of California, San Diego, CA, USA)	N/A
Py2T murine breast cancer cell line	Gift from Dr. Gerhard Christofori (University of Basel, Basel, Switzerland)	N/A
NCTC clone 929 (L-929)	ATCC	CCL-1
bEnd.3 murine endothelial cell line	ATCC	CRL-2299

Continued		
REAGENT or RESOURCE	SOURCE	IDENTIFIER
Experimental models: Organisms/strains		
C57BL/6J (B6)	The Jackson Laboratory	Strain#000664
FVB/NJ (FVB)	The Jackson Laboratory	Strain#001800
B6.Cg-Tg(CAG-DsRed*MST)1Nagy/J (DsRed)	The Jackson Laboratory	Sarin#006051
B6.129S4-Ptgs2tm2.1Hahe/J (Cox2$^{luc/luc}$)	The Jackson Laboratory	Strain#030853
B6.129-Ptger2tm1Brey/J (EP2 KO)	The Jackson Laboratory	Strain#004376
Oligonucleotides		
Primer for RT-qPCR	Integrated DNA Technologies	Table S4
Primer for Genotyping	Integrated DNA Technologies	Table S4
Software and algorithms		
Living Image Analysis software version 4.7.3	PerkinElmer	N/A
GraphPad Prism software version 10.0.0	GraphPad Software	N/A
Aperio ImageScope software version 12.4.3.7001	Leica Biosystems	N/A
ZEN lite software version 3.3.89.0000	Carl Zeiss Microscopy	N/A
ImageJ software version 1.53i	National Institutes of Health	N/A
Wound healing size plugin for ImageJ		https://doi.org/10.1371/journal.pone.0232565
FlowJo software version 10.8.0	Becton Dickinson	N/A
SAS 9.4	SAS Institute	N/A
JMP 16.0.0.	SAS Institute	N/A
R version 4.1.2	R Development Core Team	N/A
BioRender	BioRender	N/A
Adobe Illustrator 28.0	Adobe	N/A

RESOURCE AVAILABILITY

Lead contact
Further information and requests for resources and reagents should be directed to and will be fulfilled by the lead contact, Takemi Tanaka (Takemi-Tanaka@ouhsc.edu).

Materials availability
This study did not generate new and unique reagent. Cell lines can be shared upon reasonable request from the lead contact without restriction.

Data and code availability
- RNA-sequence data was uploaded to the NCBI Sequence Read Archive (accession number: PRJNA1031635).
- This study does not contain original code.
- Any additional information required to reanalyze the data reported in this study is available from the lead contact upon request.

EXPERIMENTAL MODEL AND STUDY PARTICIPANT DETAILS

Human cohort
Stage I-II breast cancer cases diagnosed from 2007 to 2017 were analyzed using the National Cancer Database (NCDB). NCDB is a joint project of the Commission on Cancer (CoC) of the American College of Surgeons and the American Cancer Society. The CoC's NCDB and the hospitals participating in the CoC NCDB are the source of the de-identified data used herein; they have not verified and are not responsible for the statistical validity of the data analysis or the conclusions derived by the authors. The NCDB is publicly available; this study was approved by the University of Oklahoma Health Sciences Center Institutional Review Board committee (#7446) with consent waived. The primary exposure examined was the continuous biopsy-to-surgery interval (days) and the primary outcome was the overall mortality. Covariate balancing propensity score weights were calculated with the biopsy-to-surgery interval as a continuous endpoint and adjusted for age, race, Charlson comorbidity score, stage, grade, histology, hormone receptor status, and treatment (endocrine, chemotherapy/targeted therapy, and radiation). A Cox proportional hazard model was used to fit a flexible natural cubic spline of the biopsy-to-surgery interval and adjusted by normalized inverse propensity score weights. Hazard ratios were computed with day 30 as the reference, and simultaneous 95% confidence limits. p-values were adjusted for multiple comparisons using the Scheffe method. The adjusted Cox proportional hazard model was used to

calculate the cumulative hazard function across survival time for specific biopsy-to-surgery intervals conditional on the most common value of other covariates. Adjusted mortality probability from this plot was compared between different biopsy to surgery intervals (e.g., 14-year mortality).

In addition, formalin-fixed paraffin-embedded (FFPE) whole-mount blocks were collected from tissue archives from the University of Oklahoma Health Sciences Center under approval by the Institutional Review Board committee (#3597). Informed consent was obtained from all patients prior to tissue procurement for diagnostic purposes. This study was granted exempt category 4 and no PHI was involved in this study. Stage I-II ER$^+$ ductal carcinoma cases that underwent needle biopsy for definitive diagnosis followed by surgery from 2015 to 2020, with no history or concurrent cancer diagnosis, were identified for immunohistochemistry. Clinical (biopsy-to-surgery interval, stage, histology grade and subtypes) and demographic (age and race) information were obtained by electronic medical chart review.

Cell culture

Py230 murine breast cancer cells were cultured in Ham's F-12K (Kaighn's) Medium (Thermo Fisher Scientific, Waltham, MA, USA) supplemented with 5% fetal bovine serum (FBS), 1% antibiotic-antimycotic (Thermo Fisher Scientific) and 0.1% MITO+ Serum Extender (Corning, NY, USA). Py2T murine breast cancer cells were cultured in Dulbecco's Modified Eagle Medium (DMEM; Thermo Fisher Scientific) supplemented with glutamine (Thermo Fisher Scientific), 10% FBS, and 1% antibiotic-antimycotic (Thermo Fisher Scientific). These cell lines were transduced with mCherry Lentifect lentiviral particles (GeneCopoeia, Rockville, MD, USA) and selected with 0.3 μg/mL puromycin. Bend.3 cells were cultured in low sodium bicarbonate (1.5 g/L) DMEM supplemented with glutamine (Thermo Fisher Scientific), 10% FBS, and 1% antibiotic-antimycotic (Thermo Fisher Scientific). Macrophages (Mφ) were isolated from the bone marrow of female B6 mice and enriched in Eagle's Minimum Essential Medium (EMEM) supplemented with 10% FBS, 1% antibiotic-antimycotic, and 20% L929-cell conditioned media. All cells were cultured in humidity chambers at 37°C under normoxia (20% O_2, 5% CO_2, 75% N_2) or hypoxia (5% O_2, 5% CO_2, 90% N_2). Hypoxia was achieved using Hypoxia Incubator Chamber (STEMCELL Technologies, Vancouver, BC, Canada).

Breast tumor mouse models

All mouse experiments in this study were approved and performed in accordance with the guidelines and regulations of Institutional Animal Care and Use Committee of the University of Oklahoma Health Sciences Center (19-027-SCHU, 20-040-SCHXU, 20-077-SCHXU). All mice were purchased from Jackson Laboratory (Bar Harbor, ME, USA) and maintained in a pathogen-free barrier facility. Py230 or Py2T cells at a density of 2 x 10^6 cells per 100 μL in a 1:1 mix of RPMI-1640 and Matrigel GFR (Corning) were injected into the abdominal mammary fat pad of 6-week-old female B6 or FVB mice, respectively. Tumor size was measured by caliper every three days, and tumor volume was calculated using the formula L × W^2 × 0.5, where L is the long diameter, and W is the short perpendicular diameter. Needle biopsy of tumors was performed using a vacuum-assisted biopsy device once tumor volume reached approximately 100 mm^3. A 22G needle connected to the device was inserted horizontally at 5 mm depth and slowly removed once the pressure reached −70 kPa. To examine the effect of NISADs, the mice were fed *ad-libitum* with a dough diet (Transgenic Dough Diet; Bio-Serv) containing either Celecoxib (200 mg/kg; Cayman Chemical, Ann Arbor, MI, USA), PF04418948 (50 mg/kg; Cayman Chemical), or corn oil from one day after the biopsy until the study endpoint.

METHOD DETAILS

Whole bone marrow adoptive transfer for *in vivo* COX-2 promoter assay

Adoptive transfer was achieved by intravenous injection of whole bone marrow-derived cells (BMDCs) isolated from the hind limbs of female donor mice (B6; 129S4-Ptgs2tm2.1Hahe/J [Cox-2 luc/luc] or non-carrier [wt]) into C57BL/6J recipient mice. The recipient mice were treated with sulfamethoxazole (0.96 mg/mL) and trimethoprim (0.192 mg/mL) in drinking water for three days prior to whole-body irradiation at 1000 cGy using X-RAD320 (Precision X-ray Irradiation, Madison, CT, USA) for two consecutive days. Three weeks later, Py230 cells were injected into the mammary fat pad as described above. Bioluminescence was measured as photon flux using IVIS *In Vivo* Spectrum Imaging System (PerkinElmer, Waltham, MA, USA) via intravenous injection of 100 μL IVISbrite D-Luciferin (15 mg/mL; PerkinElmer) before (as time 0) and after biopsy at indicated time points. Images were visualized using Living Image Analysis Software version 4.7.3 (PerkinElmer).

Mφ adoptive transfer

Recipient mice bearing Py230 tumors (approximately 100 mm^3 in size) were intraperitoneally injected with clodronate liposomes (100 mg/kg; Liposoma, Amsterdam, The Netherlands) to deplete Mφ. Two days later, the mice received a needle biopsy immediately after receiving adoptive transfer of Mφ isolated from female donor mice (B6.129-Ptger2tm1Brey/J [EP2−/−], non-carrier [wt], or B6.Cg-Tg(CAG-DsRed*MST)1Nagy/J).

In vivo hypoxia assay

Mice were fed with chlorophyll free diet (AIN-76A, Bio-Serv, Flemington, NJ, USA) throughout the study period. Hypoxisense 680 (100 μL; PerkinElmer) was intravenously injected into the Py230 tumor bearing mice at indicated time points. Fluorescence from

tumor and background was measured 24 h later using IVIS Spectrum imaging system at Ex675/Em720 and Ex570/Em720, respectively. Images were analyzed using Living Image Software.

Immunohistochemistry

Histopathologic analysis was performed on FFPE sections (4 μm) and O.C.T. compound (Sakura Finetek, Torrance, CA, USA) embedded frozen sections (10 μm thickness). For FFPE sections, following deparaffinization and hydration, antigen retrieval was achieved at 110°C for 15 min or 95°C for 20 min using Envision Flex Target Retrieval Solution (pH 6.1, Dako, Santa Clara, CA, USA) for mouse and human tissues, respectively. The slides were blocked with Peroxidazed 1, Background Sniper (Biocare Medical, Pacheco, CA, USA), and then incubated with primary antibody followed by the respective HRP secondary antibody. The slides were then visualized with Betazoid DAB Chromogen (Biocare Medical) and then counterstained with CAT hematoxylin. For chromogenic staining of mCherry, Vulcan Fast Red Chromogen (Biocare Medical) was used for visualization, following MACH 2 Rabbit AP-Polymer (Biocare Medical), in TBS buffer. The slides were scanned using Aperio slide scanner (Leica Biosystems, Nussloch, Germany) and image data were quantified using Aperio ImageScope software Version 12.4.3.7001 (Leica Biosystems) or scanned using ZEISS Axio Scan.Z1 Digital Slide Scanner (Carl Zeiss Microscopy, Oberkochen, Germany), using 40x objective. Image data were acquired using ZEN lite software (Carl Zeiss Microscopy), and quantified using ImageJ (NIH, Bethesda, MD). For multicolor immunofluorescence staining, following the secondary antibody, the slides were quenched with TrueVIEW Autofluorescence Quenching Kit (Vector Laboratories, Newark, CA, USA), counterstained with DAPI, and mounted with Vectashield antifade mounting medium (Vector Laboratories). Fluorescently stained slides were scanned using ZEISS Axio Scan.Z1 Digital Slide Scanner (Carl Zeiss Microscopy), using 40x objective. Image data were acquired using ZEN lite software (Carl Zeiss Microscopy), and quantified using ImageJ (NIH). For frozen section of tumor derived from mice with DsRed Mφ adoptive transfer, the slides were incubated with 10% buffered formalin, Background Sniper (Biocare Medical), followed by Alexa Fluor 488 anti-mouse CD206 antibody (BioLegend, San Diego, CA, USA). For histologic quantification of local hypoxia, pimonidazole (Hypoxyprobe, Burlington, MA, USA) was injected 2 h before tumor resection. Frozen sections were fixed in cold acetone, blocked with Background Sniper, incubated with mouse monoclonal anti-pimonidazole antibody (Hypoxyprobe), and then anti-mouse Alexa Flour Plus 488 secondary antibody (Thermo Fisher Scientific) following manufacturer's instruction. The slides were counterstained with DAPI and mounted with Vectashield. For spatial comparison, adjacent and distant were defined as areas within 500 μm and >3 mm away from the border of biopsy wound, respectively.

Multiplex immunofluorescent imaging for clinical cases

Multiplex immunofluorescence staining was performed with Opal 6-Plex Detection Kit (NEL871001KT; Akoya Biosciences, Marlborough, MA) using 6 Opal dyes along with Spectral DAPI counterstain. FFPE tissue samples were prepared for staining by baking at 60°C for 1 h followed by three 10-min washes in xylene to remove paraffin. Samples were rehydrated via an ethanol gradient into deionized water. A six-step cycle of heat-induced epitope retrieval, blocking, primary antibody incubation, Polymer HRP mouse + rabbit secondary antibody incubation, Opal dye-conjugated tyramide deposition, and antibody stripping was performed for each of the six tissue biomarkers using a Leica BOND RX fully automated research stainer (Leica Biosystems). Slides were mounted with coverslips using ProlongGold and multispectral detection and imaging was performed using the PhenoImager HT System (Akoya). Analysis of the data was performed using InForm cell analysis software. A core biopsy wound is defined as a space or tract surrounded by fibrotic and/or cystic changes with inflammatory changes that follows the shape of the biopsy trocar used in the initial diagnostic biopsy. Adjacent and distant were defined as areas within 400 μm and >3 mm away from the border of biopsy wound, respectively.

Immunofluorescence of cultured cells

Following a brief fixation with 4% paraformaldehyde, the slides were incubated with primary antibodies (listed in Supplementary Information), followed by corresponding fluorophore-conjugated secondary antibodies. Images were acquired using Leica DM 2500 using 40x objective or Leica SP8 confocal microscope using 40x objective.

Multicolor flow cytometry for Mφ immunoprofile

For immune-profiling, tumors were cut into small pieces (1 mm^3), treated with 1 mg/mL collagenase A (MilliporeSigma, Burlington, MA, USA) and 250 units/mL DNase I (MilliporeSigma) at 37°C for 30 min, and filtered through a 40 μm strainer. The homogenate was layered onto Lympholyte M (CEDARLANE, Burlington, NC, USA). Buffy coat was incubated with Zombie Aqua viability kit (Biolegend), Fc-block (Biolegend), followed by the primary antibodies. Following fixation with FluoroFix Buffer (Biolegend), the data were collected on the FACSCelesta instrument (BD Biosciences, San Jose, CA, USA), analyzed by the BD FACSDiva software (BD Biosciences) and the FlowJo software version 10 (BD Biosciences). To quantify mCherry expressing breast cancer cells, the lungs were digested with 62.5 μg/mL Liberase (MilliporeSigma) and 500 units/mL DNase I (MilliporeSigma). The cell suspension was incubated with Zombie Aqua viability kit (Biolegend) and analyzed using a S1000EON benchtop flow cytometer (Stratedigm, San Jose, CA, USA).

qRT-PCR of Mφ

The primary Mφ were treated with 100 ng/mL LPS (MilliporeSigma) and 20 ng/mL interferon-γ (IFN-γ) (Tonbo Biosciences, San Diego, CA, USA) for 8 h to polarize toward M1. The resulting M1φ were treated with 100 nM Prostaglandin E2 (Cayman Chemical)

for 24 h. Total RNA was isolated using TRIzol (Thermo Fisher Scientific). cDNA was synthesized using ProtoScript II First Standard cDNA Synthesis Kit (New England Biolabs, Ipswich, MA, USA) and subjected to qPCR using SYBR Green qPCR Master Mix (MedChemExpress, Monmouth Junction, NJ, USA) and the CFX96 Touch Real-Time PCR Detection System (Bio-Rad, Hercules, CA, USA) with primers listed in Table S4. Data were presented as delta-Ct relative to GAPDH.

Illumina RNA-seq libraries

Total RNA was isolated from the primary Mφ using TRIzol (Thermo Fisher Scientific) and cleaned with Quick-RNA MicroPrep Kit (Zymo Research, Irvine, CA, USA) following the vendor's instructions. RNA quality and quantity were determined using 2100 Bioanalyzer (Agilent) and NanoDrop (ThermoFisher), respectively. Stranded RNA-sequence libraries were prepared from 1 μg RNA using NEBNext Poly(A) mRNA isolation kit (New England Biolabs) and xGen Broad-Range RNA Library Prep Kit (Integrated DNA Technologies) Prior to sequencing, the size and quality of the libraries was confirmed using Qubit 4 fluorometer (Invitrogen) and 2100 Bioanalyzer, the samples were normalized and pooled onto a 2 x 150 bp paired-end run on NextSeq 2000 Sequencing System platform (Illumina) with a targeted sequencing depth of 50 M reads per sample. Basic data analysis was performed using pipelines on Illumina's BaseSpace Sequence Hub and aligned to GRCm38 genome assembly with differential gene expression performed using DESeq2.

Western blotting

Small piece of tumor (1 mm^3) in ice-cold RIPA buffer containing protease inhibitor cocktail (MilliporeSigma) was homogenized with 1.5 mm zirconium beads (Benchmark Scientific, China) at 4000 RPM for 20 s (Beadbug Benchtop homogenizer, Benchmark Scientific, China). The homogenates were centrifuged at 14,000 RPM for 1 min at 4°C. The protein concentrations were quantified using Micro BCA Protein Assay Kit (Thermo Fisher Scientific). Thirty micrograms protein was resolved on 8–10% SDS-PAGE gel. PVDF membranes were blocked with 5% (w/v) non-fat dry milk and probed with primary antibodies with gentle shaking at 4°C overnight, corresponding HRP-conjugated secondary antibodies, and then with ECL (GE Healthcare, UK).

ELISA

Tumor homogenate in homogenate buffer (0.1 M phosphate buffer (pH 7.4), 1 mM EDTA, 10 μM indomethacin, protease inhibitor cocktail, 0.005% butylated hydroxytoluene) was mixed with acetone (80% v/v) and spun down at 14,000 RPM. The supernatant was concentrated with nitrogen gas and purified with MonoSpin C18 (GL science, Tokyo, Japan). The eluant was used for ELISA assay to quantify PGE2 following the vendor's instructions (514010; Cayman Chemical). Data was expressed as pg per mg of tumor. For isolation of tumor interstitial fluid, small pieces of tumor were homogenized gently using loose pestle and spun down at 14,000 RPM. The supernatants were used for ELISA assay to quantify VEGF and TGF-β1 following the vendor's instruction (ELM-VEGF; RayBio, 437707; Biolegend). Data was expressed as pg per mL tumor interstitium with mean ± SEM.

Would healing assay

Py230 cells were plated onto the 2 well culture insert (Ibidi, Gräfelfing, Germany). The cells were pre-treated with 10 μM Cytosine β-D-arabinofuranoside hydrochloride (MilliporeSigma) for 1 h, followed by condition medium collected from Mφ treated with or without PGE$_2$ under hypoxia (5% O$_2$) for 12 h. Images captured by light microscope at 10x magnification were analyzed by ImageJ (NIH) with "Wound healing size plugin for ImageJ" (https://doi.org/10.1371/journal.pone.0232565). The rate of migration in 12 h was expressed as the percentage of remaining scratched area compared to time 0.

Tube formation assay

BEnd.3 cell suspension was mixed with Mφ condition medium, layered onto Matrigel GFR (Corning) in 8-well glass chamber slide (Ibidi). The slides were maintained under hypoxic condition at 37°C on slide heater connected to 5% O$_2$ (Ibidi). Eight hours later, the slides were fixed and number of tubes were counted under the light microscope at 10x magnification.

QUANTIFICATION AND STATISTICAL ANALYSIS

Two group comparisons were done using the t-test, if the assumptions of normal distribution was appropriate. Otherwise, the Wilcoxon test was used instead. Two-way ANOVA was used to compare multiple groups. Data obtained from experiments were statistically analyzed to provide 95% power for a test's significance level of 0.05, CI = 95%. All statistical analyses were performed using Prism 7. (GraphPad Software, La Jolla, CA, USA), R 4.1.2 (R Foundation for Statistical Computing, Vienna, Austria), and SAS (SAS Institute, Cary, NC, USA).

Supplemental information

Needle biopsy accelerates pro-metastatic

changes and systemic dissemination in breast

cancer: Implications for mortality by surgery delay

Hiroyasu Kameyama, Priya Dondapati, Reese Simmons, Macall Leslie, John F. Langenheim, Yunguang Sun, Misung Yi, Aubrey Rottschaefer, Rashmi Pathak, Shreya Nuguri, Kar-Ming Fung, Shirng-Wern Tsaih, Inna Chervoneva, Hallgeir Rui, and Takemi Tanaka

Supplementary Information

Needle biopsy accelerates pro-metastatic changes and systemic dissemination in breast cancer: Implications for mortality by surgery delay

Hiroyasu Kameyama, Priya Dondapati, Reese Simmons, Macall Leslie, John F. Langenheim, Yunguang Sun, Misung Yi, Aubrey Rottschaefer, Rashmi Pathak, Shreya Nuguri, Kar-Ming Fung, Shirng-Wern Tsaih, Inna Chervoneva, Hallgeir Rui, and Takemi Tanaka

Lead Contact:

Takemi Tanaka, Ph.D., Professor
University of Oklahoma Health Sciences Center, School of Medicine, Dept. of Pathology,
Stephenson Cancer Center at 975 NE 10th St, BRC-W, Rm 1415, Oklahoma City, OK 73104
Email: takemi-tanaka@ouhsc.edu
Phone: Office (405)-271-8260

This PDF included Figure S1-S7 and Table S1-S4

Figure S1

A

Py230^mCherry

Brightfield | Fluorescence

100 μm | 100 μm

Py2T^mCherry

Brightfield | Fluorescence

100 μm | 100 μm

B

Py230^mCherry Tumor (15-day post-biopsy)

Adjacent | Distant

BW

200 μm | 200 μm

Py2T^mCherry Tumor (15-day post-biopsy)

Adjacent | Distant

BW

200 μm | 200 μm

Brown: anti-mCherry   Blue: hematoxylin

C

Py230^mCherry (B6)

Gate | Tumor volume

Biopsy(+)

Biopsy(-)

TxRed | FITC

Biopsy (−)
Biopsy (+)

Log Tumor Volume
Post-biopsy time (days)

Body weight

ns

Body weight (g)
Biopsy − +

Py2T^mCherry (FVB)

Gate | Tumor volume

Biopsy(+)

Biopsy(-)

TxRed | FITC

Biopsy (−)
Biopsy (+)

Log Tumor Volume
Post-biopsy time (days)

Body weight

ns

Body weight (g)
Biopsy − +

D

Py230^mCherry → 30 days → Biopsy → 6 hours → Whole Blood collection for FACS

WBC

Py230^mCherry | Py230^mCherry

WBC

TxRed | FITC

mCherry+ cells in blood (count)
Biopsy − +

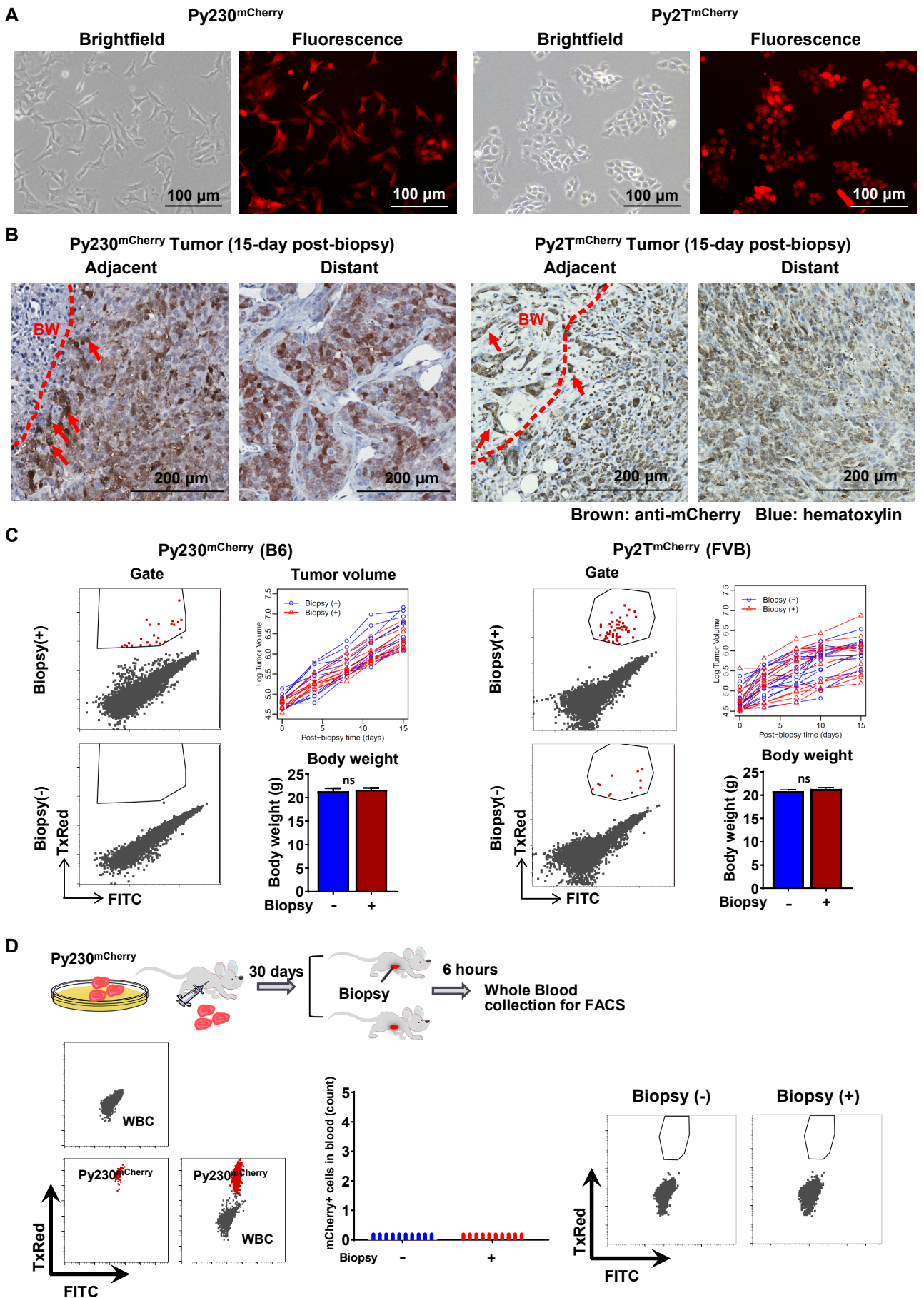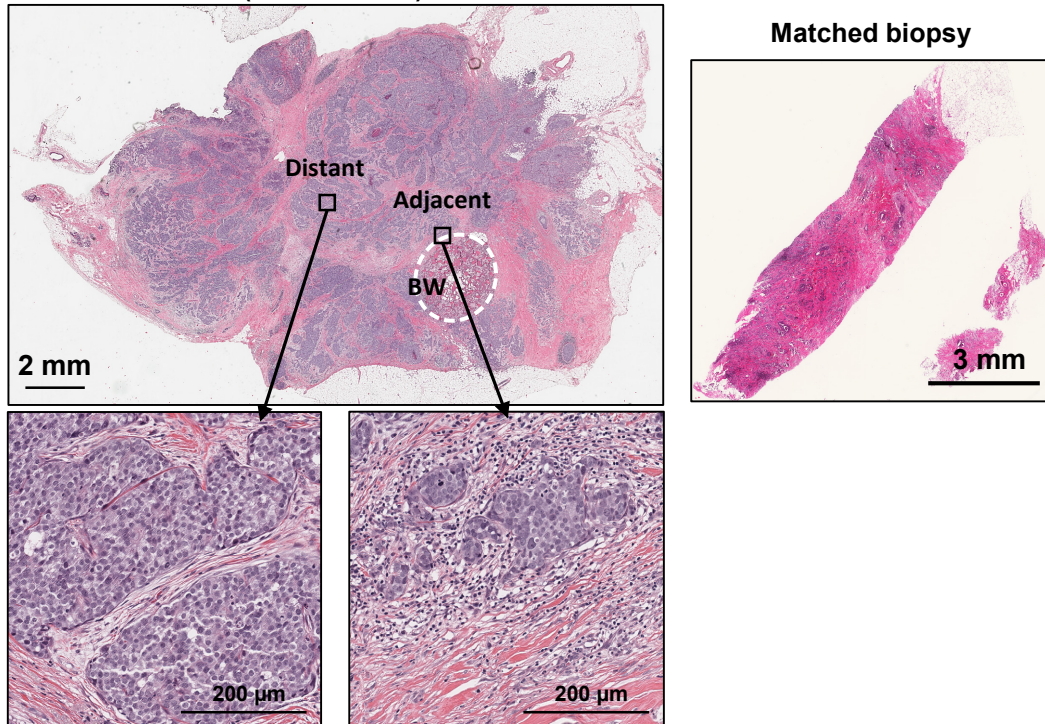**Biopsy (-)** | **Biopsy (+)**

TxRed | FITC

**Figure S1. Needle biopsy of breast tumor does not cause cancer cell displacement, related to Figure 1.**
(A) Brightfield and fluorescent images of Py230^{mCherry} and Py2T^{mCherry} mouse mammary carcinoma cells. (B) Immunohistochemical staining of mCherry (brown) in 15-day post-biopsy Py230^{mCherry} and Py2T^{mCherry} tumors both adjacent (left) to and distant (right) from biopsy wound. The slides were counterstained with Hematoxylin (blue). Red arrows indicate spindle-shaped mCherry+ cancer cells adjacent immediately outside of the wound; the red dotted line indicates the boundary of the biopsy wound. BW: biopsy wound. (C) Representative images of flow cytometric analyses of mCherry-positive BC cells after scatter gating and live cell gating of whole lung of Py230^{mCherry} and Py2T^{mCherry} tumors. The growth rate of Py230^{mCherry} and Py2T^{mCherry} tumors derived from mice assigned to study in Figure 1E (n=10-13) and 1F (n=11-12), respectively. Tumor volume of each mouse was plotted over post-biopsy days (biopsy as day 0); *P*-values were calculated using Student's T-test. The endpoint bodyweight of the mice assigned to this study; *P*-values were calculated using Student's T-test. (D) The absence of disseminated Py230^{mCherry} cells in the circulation after tumor biopsy. Whole blood was collected from B6 mice by cardiac puncture 6 hours following biopsy of the Py230^{mCherry} tumor. Following red blood cell lysis, a single cell suspension of white blood cells (WBCs) was analyzed by flow cytometry (n=10). Flow cytometry gating shows WBCs (gray), Py230^{mCherry} cells (red), and Py230^{mCherry} and WBC mixture. The graph depicts the absence of Py230^{mCherry} cells in the whole blood 6 hours after the biopsy. Representative flow cytometry gating indicates the absence of Py230^{mCherry} cells in the peripheral blood regardless of biopsy.

Figure S2

A
25-day post-biopsy surgical resected clinical BC (whole mount)

Matched biopsy

B
15-day post-biopsy Py230 tumor (whole mount)

Matched biopsy

C
15-day post-biopsy Py230 tumor
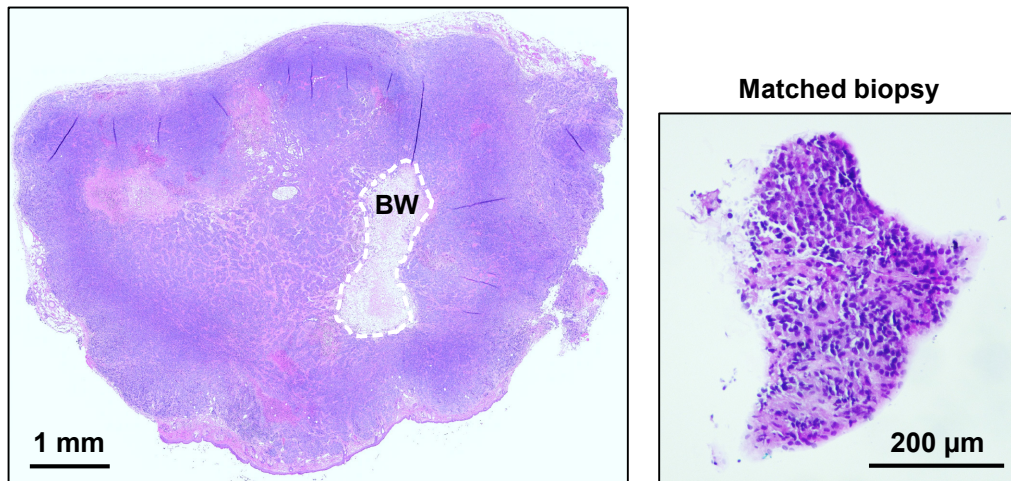
CK14
Adjacent   Distant

CK17
Adjacent   Distant
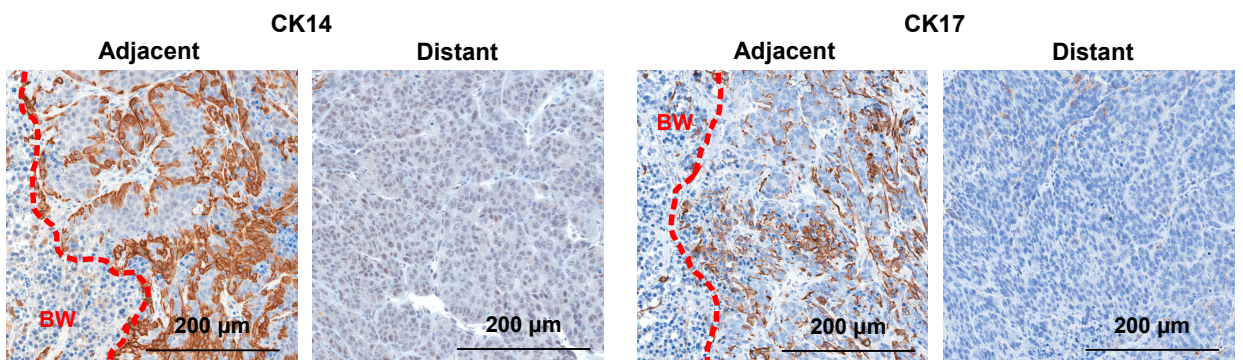
Brown: anti-CK14 or anti-CK17 Blue: hematoxylin

Figure S2. Prolonged retention of inflammatory cells adjacent to biopsy wound, related to Figure 2.

(A) Representative H&E image shows the whole mount of surgically resected tumor and the matched biopsy of tumor used for Fig. 2A. The white dotted line indicates the border of the biopsy wound (BW). High-power magnification images of adjacent and distant areas correspond to fluorescent images shown in 2A. (B) H&E image of 15-day post-biopsy Py230 tumor and vertical section of the matched biopsy used for Fig. 2D. The white dotted line indicates the border from the biopsy wound (BW). (C) Immunohistochemical staining of CK14 and CK17 (brown) in 15-day post-biopsy Py230^{mCherry} tumors both adjacent (left) to and distant (right) from the biopsy wound. Red dotted line indicates the border of biopsy wound (BW).
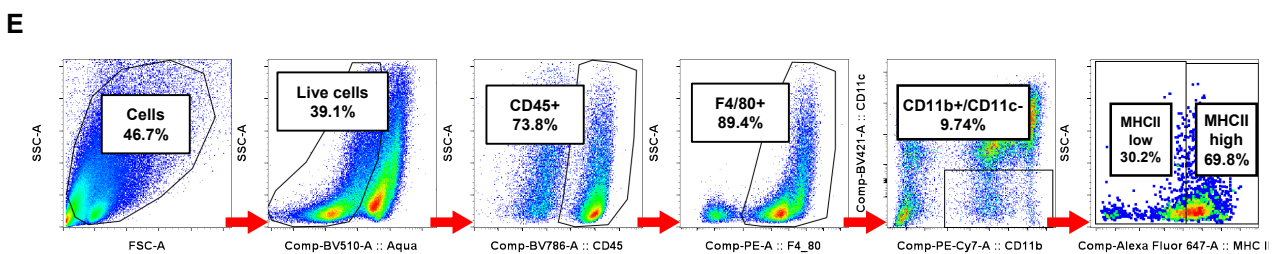
Figure S3

A

Biopsy(-) Parenchyma | **Biopsy(+) Distant** | **Biopsy(+) Adjacent**

F4/80

Mark-up image

50 μm

P<0.001

F4/80 (% of total cell count)

Dist | Adja

Yellow: Cytoplasm **Navy**: F4/80 Positive **Light blue**: F4/80 Negative

Biopsy(-) Parenchyma | **Biopsy(+) Distant** | **Biopsy(+) Adjacent**

CD206

Mark-up image

50 μm

P<0.001

CD206 (% of total cell count)

Dist | Adja

Yellow: Cytoplasm **Navy**: CD206 Positive **Light blue**: CD206 Negative

B

Primary MΦ

150 μm

96.7%

Live 97.6%

CD45+ 99.5%

F480+/CD11b+ 99.7%

SSC-A / FSC-A

SSC-A / Comp-Zombie Aqua-A :: live_dead

SSC-A / Comp-PE-Cy7-A :: CD45

Comp-FITC-A :: CD11b / Comp-PE-A :: F4_80

C

H&E

2 mm

DsRed
DAPI

2 mm

200 μm

200 μm

D

1 mm

CD206

Overlay

50 μm

50 μm

10 μm

DsRed

DAPI

50 μm

50 μm

E

Cells 46.7%

Live cells 39.1%

CD45+ 73.8%

F4/80+ 89.4%

CD11b+/CD11c- 9.74%

MHCII low 30.2% MHCII high 69.8%

SSC-A / FSC-A

SSC-A / Comp-BV510-A :: Aqua

SSC-A / Comp-BV786-A :: CD45

SSC-A / Comp-PE-A :: F4_80

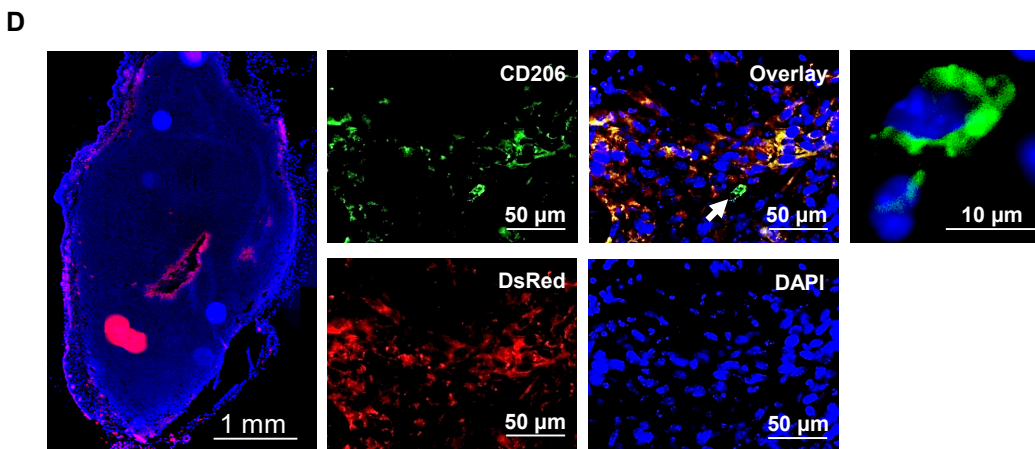Comp-BV421-A :: CD11c / Comp-PE-Cy7-A :: CD11b
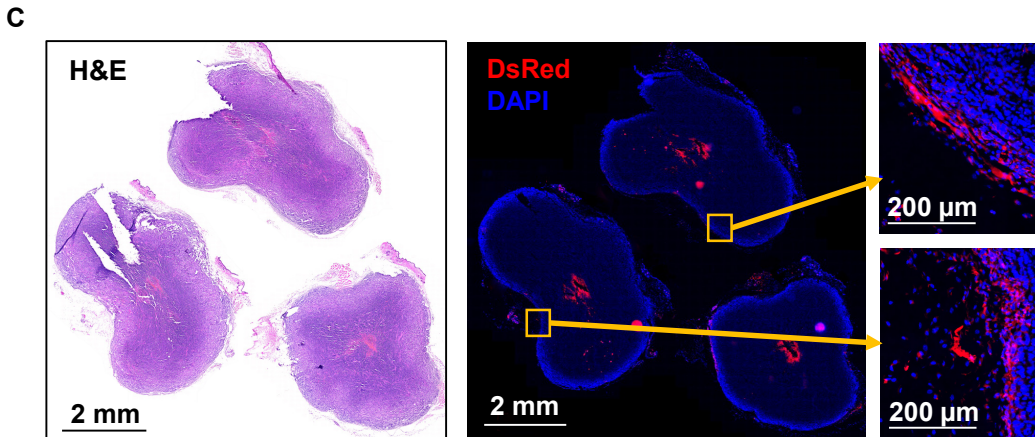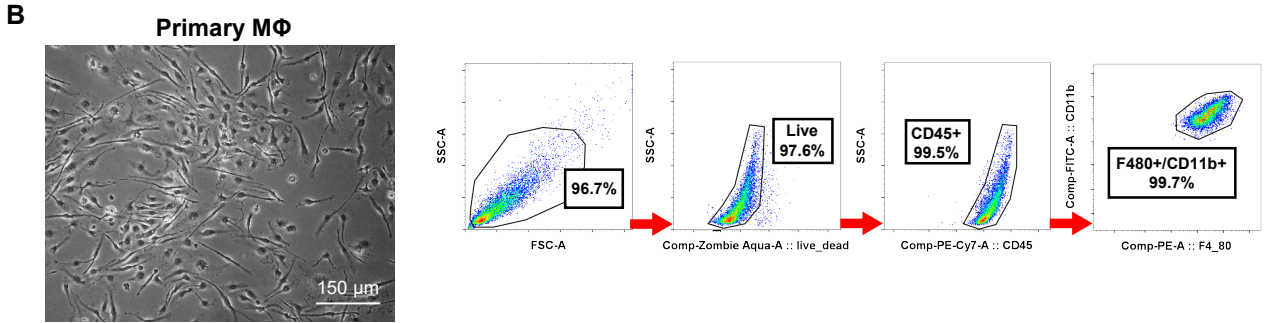
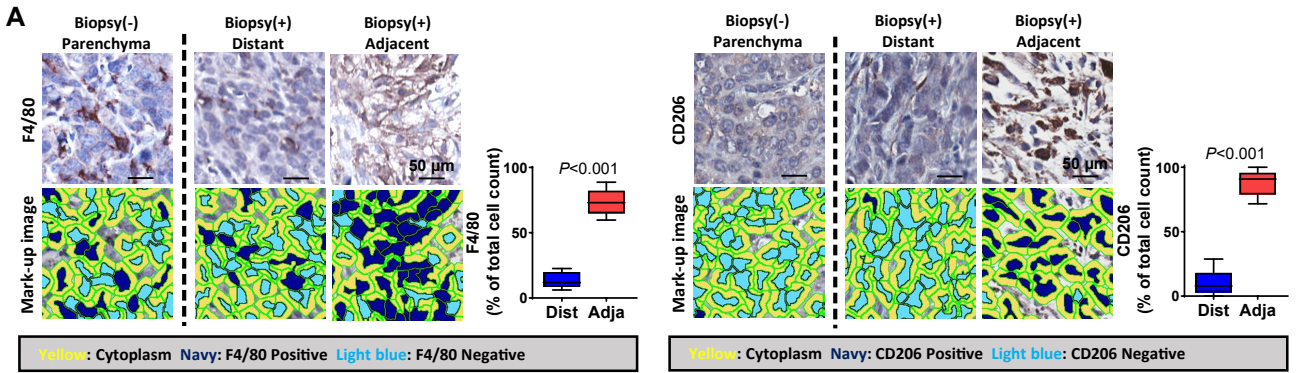SSC-A / Comp-Alexa Fluor 647-A :: MHC II

Figure S3. M2ϕ accumulation emerged as early as one day after biopsy in Py230 tumors, related to Figure 3.
(A) Algorithm used for the quantification of F4/80+ and CD206+ IHC-stained cells using Aperio Image Suite. Representative images of F4/80 and CD206 expression in unbiopsied Py230 tumor (left), distant from biopsy wound (middle), and adjacent to biopsy wound (right). Graphs depict the percentage of positive cells normalized by nucleus count (n=13). *P*-values were calculated using Wilcoxon test. (B) Brightfield image of bone marrow-derived primary Mϕ isolated from B6 female mice. Flow cytometry gating of bone marrow-derived primary Mϕ^{DsRed}. (C) Scanned image of 1-day post-biopsy Py230 tumors of mice that received Mϕ^{DsRed} adoptive transfer. The whole mount of three independent tumor images shows local accumulation of Mϕ^{DsRed} (red) around the biopsy wound (center hollow), nuclear counterstain with DAPI (blue), and corresponding H&E image. High-power images corresponding to orange squares indicate Mϕ^{DsRed} infiltration into the distant peripheral stroma. (D) Images of biopsied Py230 tumors in mice that received Mϕ^{DsRed} adoptive transfer, immunofluorescently stained with FITC-labeled anti-CD206 (green) and counterstained with DAPI (blue). White arrow indicates CD206+/mCherry- cells. BW: biopsy wound. (E) Flow cytometry gating of Mϕ immune-profiling for M1ϕ: CD45$^+$F4/80$^+$CD11b$^+$/CD11c$^-$MHC^{high} and M2ϕ: CD45$^+$F4/80$^+$CD11b$^+$/CD11c$^-$MHCII^{low}.
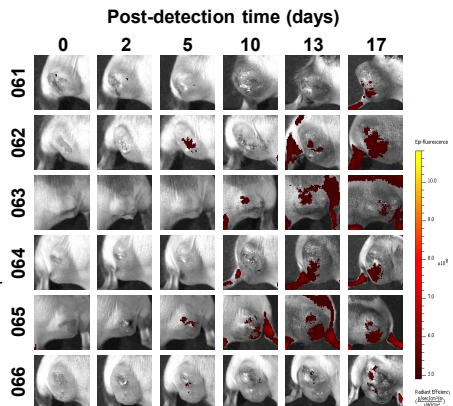
Figure S4
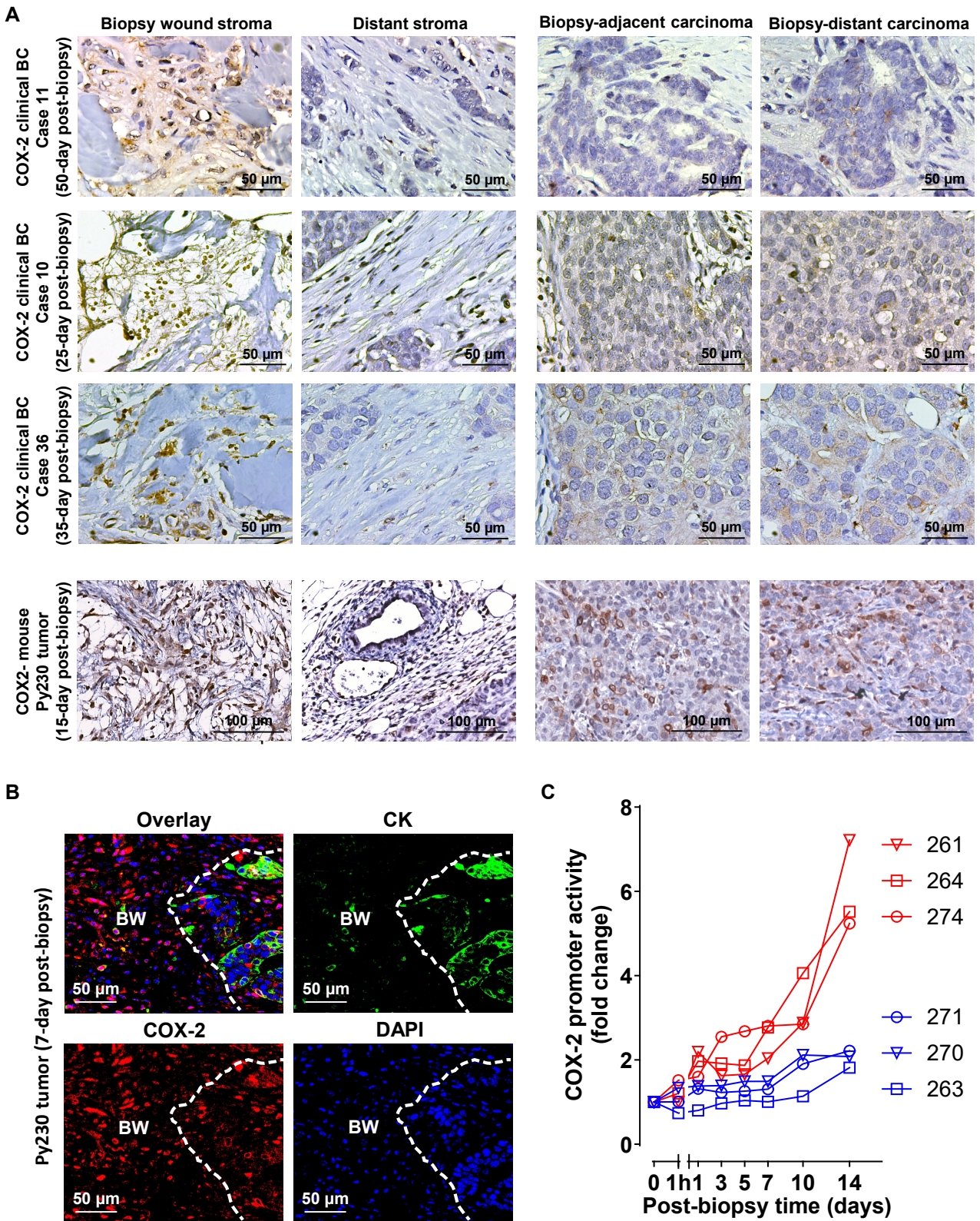
Figure S4. Sustained COX-2 activation in stromal cells in the biopsy wound, related to Figure 4.
(A) IHC staining images of COX-2 in biopsy wound stroma, peripheral stroma, carcinomas adjacent and distant from biopsy wound of three independent Stage I ER+ BC cases and 15-day post-biopsy Py230 tumor. (B) Multi-color immunofluorescent staining for CK (green), COX-2 (red), and DAPI (blue) of biopsied Py230 tumor. The white line depicts the border of biopsy wound (BW). (C) COX-2 promoter activity of individual mice before and after biopsy (red) and time-matched unbiopsied (blue) mice (n=3).

Figure S5

A

Biopsy (+)

Post-biopsy time (days)

Biopsy (-)

Post-detection time (days)

B

C

D

E

Py230 tumor (15-day post-biopsy)
TGF-ß1

Py230 tumor (7-day post-biopsy)
VEGF
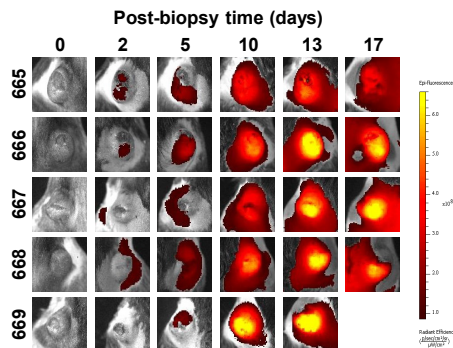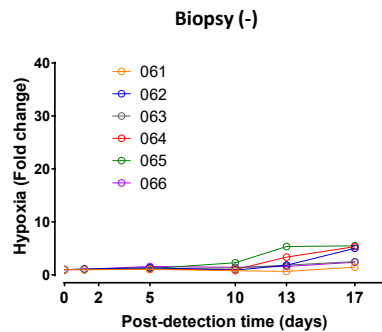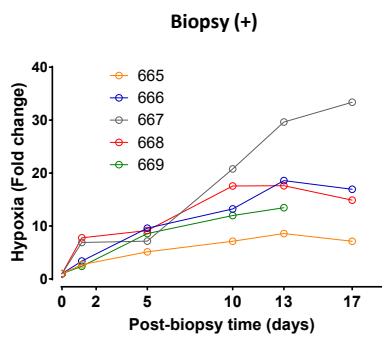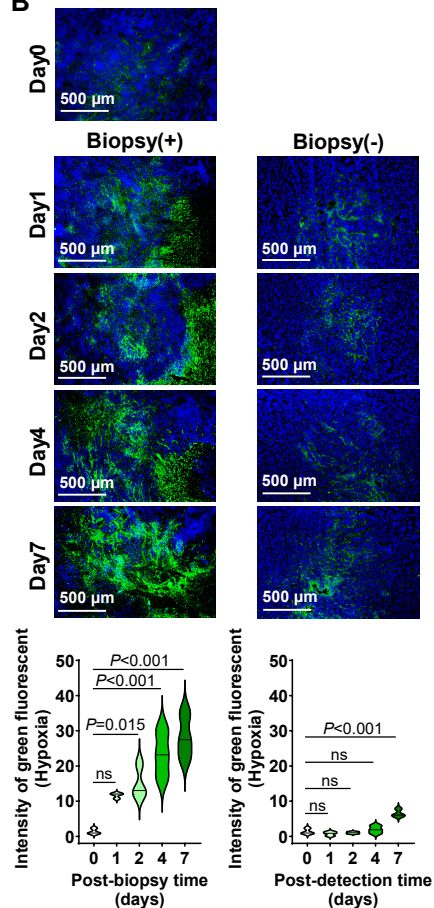
Figure S5. Biopsy of tumor instigates spatially limited but prolonged hypoxia, related to Figure 5.
(A) Hypoxia was measured at the indicated time after biopsy following the intravenous injection of HypoxySense®
using IVIS imaging system. The graph depicts fold change of photons at each time point over time 0 (before biopsy)
from individual tumors assigned to biopsy or unbiopsied control groups (n=6-7). Fluorescent images at the indicated
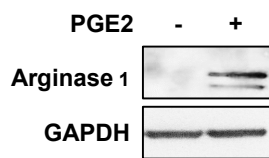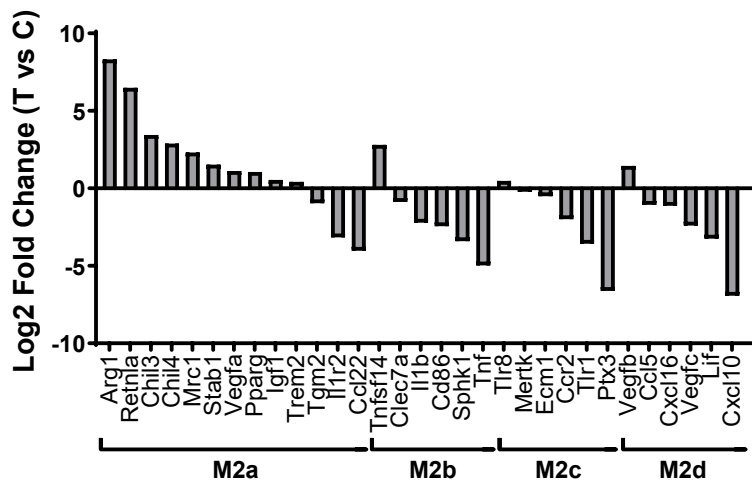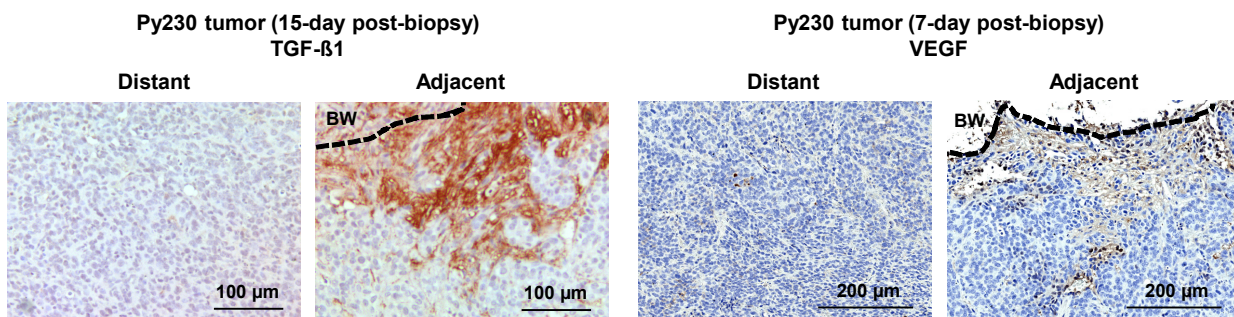time points show a flux of biopsied and unbiopsied tumors. (B) Images of biopsied Py230 tumors
immunofluorescently stained for pimonidazole. Mice assigned to biopsy or unbiopsied groups were injected with
pimonidazole HCL 2 h before tumor resection. Frozen sections were immunofluorescently stained following the
vendor's instructions (n=3). The graph depicts the quantification of hypoxia measured by pixel count normalized by
area using Image J software. P-values were calculated using one-way ANOVA, relative to time 0. (C) Western blot
of Arginase-1 from Mϕ treated with or without PGE$_2$. (D) Differential gene expression comparison of M2 subtype
associated transcripts in B6 mouse Mϕ polarized by PGE$_2$ for 24 h under hypoxia over control. The Y-axis of the bar
graph indicates the log2 fold changes of M2 subgroups associated genes in B6 mouse Mϕ polarized by PGE$_2$ for 24
h under hypoxia over control. The selected genes associated with each subtype were reported in mouse
(PMID3527030, 27683760, 27474165, 28402847, 37566293, 22730547, 32642590, 23684988). Retnla, Chil3, Chil4,
and Mrc1 results were confirmed by qRT-PCR (n=3-5) due to lower sensitivity of RNA-seq. For all transcript changes
shown, P-values <0.05. (E) IHC staining for VEGF and TGF-β1 of 7-day and 15-day post-biopsy Py230 tumors. The
black dotted line depicts the border from the biopsy wound.

Figure S6

A

B

C
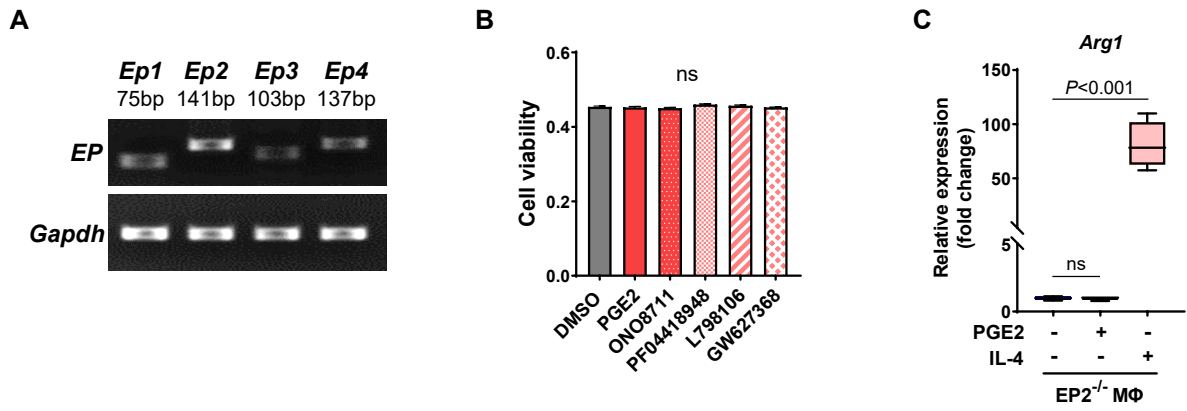
Figure S6. Absence of PGE₂-mediated M2-shift in EP2-/- Mɸ, related to Figure 6.
(A) RT-qPCR analysis for mRNA expression of prostanoid receptors (*Ep1-Ep4*) in bone marrow-derived primary Mɸ isolated from B6 mice. (B) MTT proliferation assay of Mɸ treated with EP receptor selective antagonist at a concentration of 10 nM of ONO8711 (EP1), 1 µM of PF04418948 (EP2), 10 nM of L798106 (EP3), 1 µM of GW627368X (EP4) for 24h (n=5). Data were analyzed by one-way ANOVA, relative to untreated control. (C) RT-qPCR analysis of *Arg1* expression of *Ep2⁻/⁻* Mɸ treated with PGE₂ or interleukin 4 (IL4) (n=3). *P*-values were calculated using one-way ANOVA, relative to control.

Figure S7

A

B
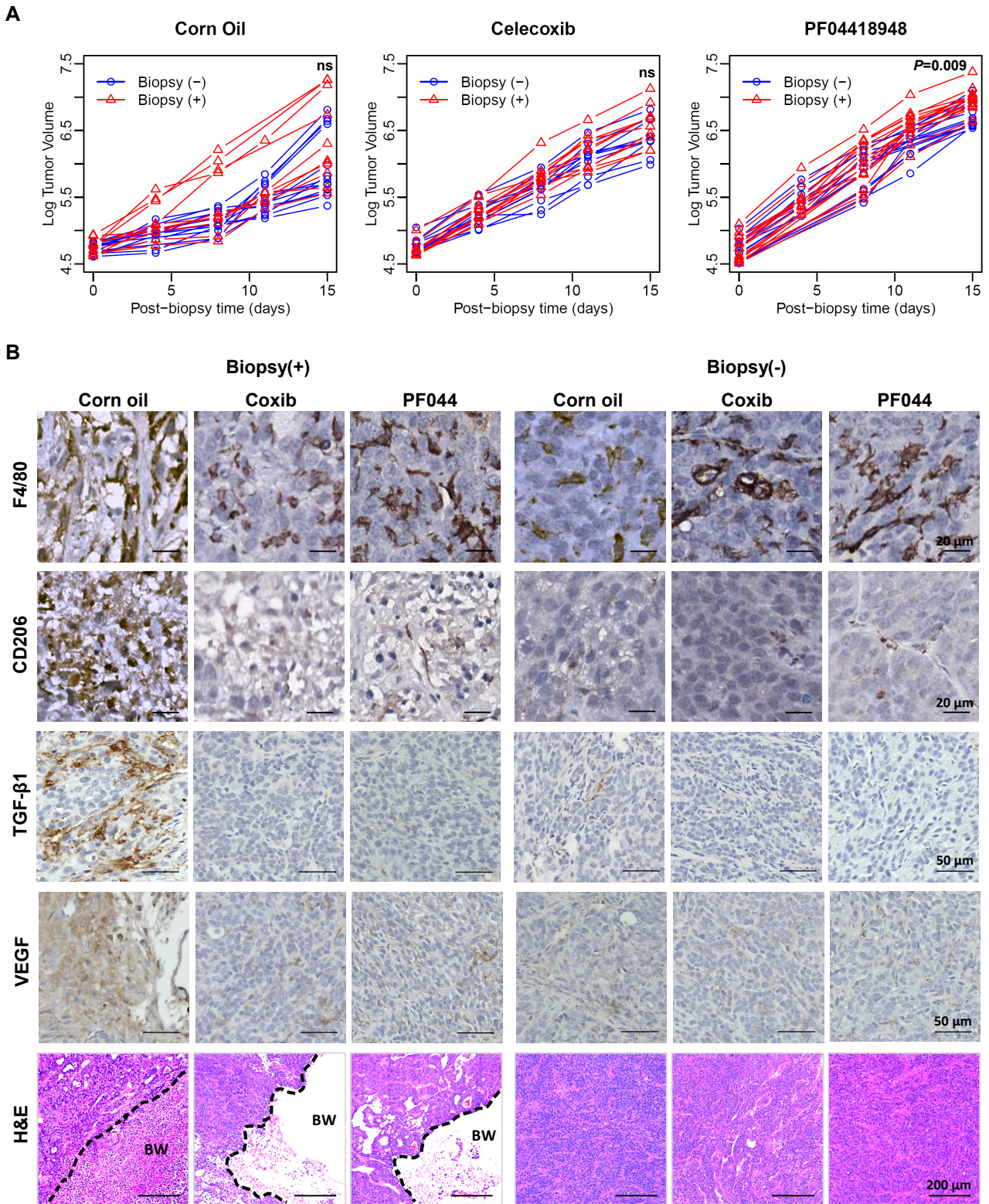
Figure S7. Oral administration of NSAIDs after biopsy inhibits biopsy-induced M2-polarization, related to Figure 7.
(A) Py230^{mCherry} tumor growth rate in mice assigned to experiments corresponding to Fig. 7A. One day after the biopsy, the mice were orally administered with either corn oil (control, n=10-11), celecoxib (n=10), or PF04418948 (n=13-15) in food *ad libitum*. The tumor volume of each mouse was plotted over post-biopsy days (biopsy as day 0). *P*-values at study endpoint were calculated using Student's T-test. (B) IHC staining images for F4/80, CD206, TGF-β1, VEGF (brown), and Hematoxylin counterstaining (blue). H&E images of biopsied or unbiopsied tumors derived from mice administered with corn oil, celecoxib, or PF04418948. The black dotted line indicates the border of the biopsy wound. BW: biopsy wound.

Table S1

Breast cancer patients, NCDB, 2004-2017 (n=2,981,732)

Breast cancer 1st and only cancer (n=2,220,634)

Exclusions:
  Male (n=19,332)
  Clinically or pathologically DCIS/LCIS or III-IV (n=1,089,951)
  Non-invasive or inflammatory histology (n=1,649)
  Diagnosis and all or part of treatment at facility other than reporting (n=572,778)
  No/missing biopsy or same day surgery (n=84,418)
  Discordant hormone receptor and endocrine treatment status (n=2,111)
  Neoadjuvant or non-definitive surgery as first treatment (n=98,032)
  No adjuvant treatment or first adjuvant treatment > 1 year post-surgery (n=16,390)
  Did not receive recommended adjuvant therapies due to contraindications or choice (n=58,510)
  Age $\geq$80 years old (n=21,194)
  Missing demographic information (n=52,864)
  Missing treatment information (n=2,244)
  No follow-up information (i.e. 2017 diagnoses; n=22,498)
  TTS =7 and >356 (n=2,200)

Clinical Stage I-II, adjuvant treated patients (n= 176,481)

Table S2

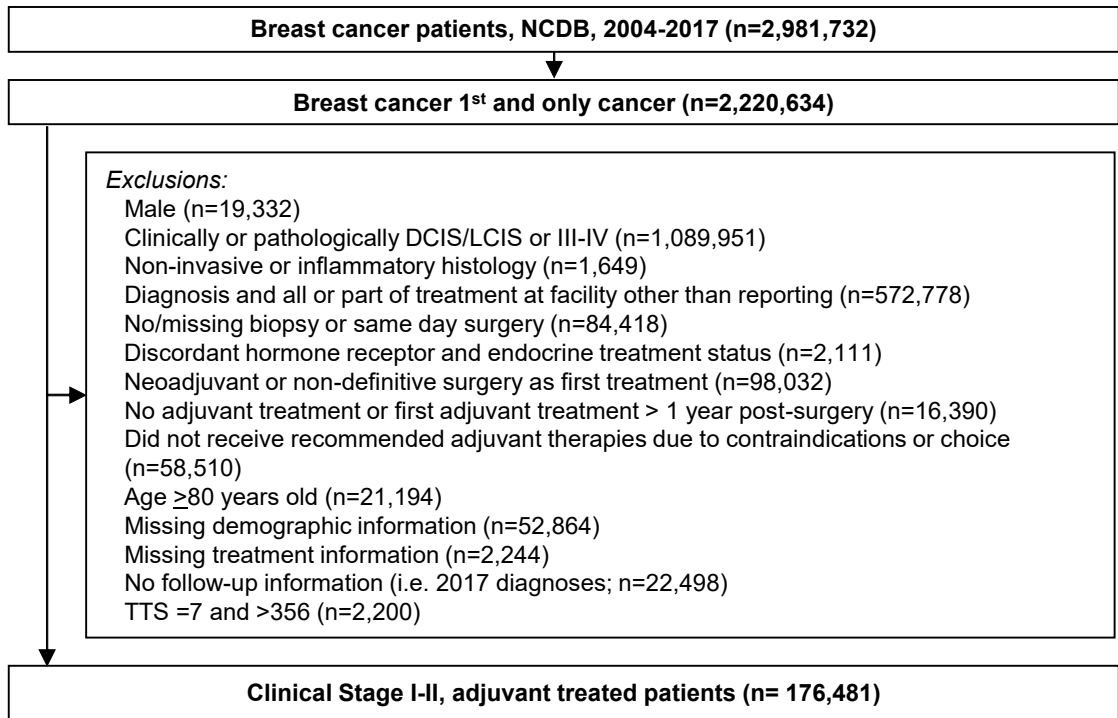**Table S2. Median and Quartiles of biopsy-to-surgery interval (days) by demographic and clinical characteristics of the cohort, related to Figure 1.**

	N (%)	Q1	Median	Q3
Overall	176481 (100)	20	28	41
Age				
<30	587 (0.33)	19	29	41
30-39	5815 (3.29)	20	29	43
40-49	28895 (16.37)	20	30	43
50-59	48421 (27.44)	20	28	41
60-69	56535 (32.03)	20	28	41
≥70	36228 (20.53)	20	28	40
Race				
White	143848 (81.51)	20	28	40
Hispanic	8523 (4.83)	24	35	51
Black	17882 (10.13)	22	34	49
Other	6228 (3.53)	21	31	45
Comorbidity				
0	147363 (83.50)	20	28	41
1	23383 (13.25)	20	29	42
=2	5735 (3.25)	21	31	44
Year of Diagnosis				
2004	3835 (2.17)	15	22	33
2005	4444 (2.52)	16	23	34
2006	5357 (3.04)	16	23	34
2007	6640 (3.76)	18	27	38
2008	12434 (7.05)	18	27	39
2009	15300 (8.67)	19	28	39
2010	15165 (8.59)	19	28	40
2011	16763 (9.50)	20	28	40
2012	16906 (9.58)	20	29	42
2013	17769 (10.07)	21	29	42
2014	19691 (11.16)	21	30	43
2015	20796 (11.78)	21	31	44
2016	21381 (12.12)	22	31	44
Clinical Stage[a]				
I	132865 (75.29)	20	28	41
II	43616 (24.71)	20	29	42
Histology Type				
Ductal	144283 (81.76)	20	28	41
Lobular	14316 (8.11)	21	31	44
Ductal and Lobular	9174 (5.20)	21	30	43
Other	8708 (4.93)	20	28	41
Histology Grade				
1	50553 (28.65)	20	29	41
2	79348 (44.96)	20	29	42
>3	46580 (26.39)	19	28	40
Type of Surgery				
Breast Conserving	125297 (71.00)	19	27	38
Mastectomy	31554 (17.88)	20	29	42
Mastectomy with Reconstruction	19630 (11.12)	28	40	54
Urban/Rural Status[b]				
Metro ≥ 1 million	90102 (51.05)	21	30	43
Metro < 1 million	60932 (34.53)	19	28	40
Urban/Rural	25447 (14.42)	17	26	36
Endocrine Therapy				
No	29983 (16.99)	19	27	39
Yes	146498 (83.01)	20	29	42
Chemotherapy/Biological				
No	104659 (59.30)	20	29	42
Yes	71822 (40.70)	19	28	40
Radiation Therapy				
No	51608 (29.24)	22	33	47
Yes	124873 (70.76)	19	27	39
Hormone Receptor				
Positive	154126 (87.33)	20	29	42
Negative	22355 (12.67)	18	27	38
Type of First Adjuvant Therapy				
Radiation	64470 (36.53)	31	42	55
Chemotherapy/BRM	67478 (38.24)	30	40	51
Endocrine Therapy	44533 (25.23)	21	33	48
Insurance type				
Not Insured	3372 (1.91)	22	34	52
Private Insurance	101483 (57.50)	20	28	41
Medicaid	10357 (5.87)	22	34	50
Medicare	52719 (29.87)	20	28	40
Other Government	8550 (4.84)	21	30	44
% No High School Degree[c]				
≥ 29%	24212 (13.72)	21	30	45
20-28.9%	36578 (20.73)	20	29	42
14-19.9%	41417 (23.47)	20	28	41
< 14%	74274 (42.09)	20	28	40
Median Income[c]				
< $30,000	18613 (10.55)	20	29	43
$30,000 – $34,999	27939 (15.83)	19	28	41
$35,000 – $45,999	48698 (27.59)	20	28	41
> $46,000	81231 (46.03)	20	29	41

a. Clinical Group Stage derived from AJCC 6th or 7th ed. Staging Manual. b. Urban/Rural Status derived from the 2000 USDA Economic Research Service Urban-Rural continuum codes. c. Education (% no high school degree) and median income quartiles for patient's ZIP-code of residence at time of diagnosis derived from year 2000 US Census data.

Table S3

A. EMT histologic analyses

Total case	12
Preoperative interval	29.4 (12-54)
Age	62.9 ± 9.7
Race	
White	9
Other	2
Unknown	1
pT	
I	10
II	2
pN	
Negative	9
Positive	3
Grade	
I	3
II	5
III	4
Luminal	
A	8
B	4

B. M2Φ histologic analyses

Total case	14
Preoperative interval	28.8 (10-54)
Age	63.1 ± 10.1
Race	
White	11
Other	2
Unknown	1
pT	
I	12
II	2
pN	
Negative	12
Positive	2
Grade	
I	4
II	7
III	3
Luminal	
A	11
B	3

Table S4

Table S4. List of primer sequences used in this study, related to STAR Methods.

RT-qPCR				
Gene	Forward Primer (5'-3')	Reverse Primer (5'-3')	Size (bp)	Tm (°C)
Arg1	CTTGCGAGACGTAGACCCTG	GCCAATCCCCAGCTTGTCTA	94	57.3
Ym1	TCATTACCCTGATAGGCATAGG	TTATCCTGAGTGACCCTTCTAAG	184	53.4
Ym2	GCTGGACCACCAGGAAAGTA	TCAGTGGCTCCTTCATTCAGA	86	55.8
LIGHT	CTGCATCAACGTCTTGGAGA	GATACGTCAAGCCCCTCAAG	205	57.9
Fizz-1	GGTCCCAGTGCATATGGATGAGACCATAGA	CACCTCTTCACTCGAGGGACAGTTGGCAGC	296	67.0
CD206	GGATTGCCCTGAACAGCAAC	ACTTAAGCTTCGGCTCGTCA	102	59.7
Gapdh	AGGTCGGTGTGAACGGATTTG	TGTAGACCATGTAGTTGAGGTCA	123	55.1

Genotyping					
Target	Name	Forward Primer (5'-3')	Reverse Primer (5'-3')	Size (bp)	Tm (°C)
COX-2	Mutant	CCATTAGCAGCCAGTTGTCA	AGCCTTATGCAGTTGCTCTC	225	F:58.2 R:58.0
	Wild type	CCATTAGCAGCCAGTTGTCA	TGCTAGAAAGGGGGTCTGAG	245	F:58.2 R:58.4
EP2	Mutant	ATTAAGGGCCAGCTCATTCC	CGTACTCCCCGTAGTTGAGC	300	F:57.6 R:59.9
	Wild type	TGCTCATGCTCTTCGCTATG	CGTACTCCCCGTAGTTGAGC	165	F:58.1 R:59.9